RSC Advances

REVIEW

View Article Online
View Journal | View Issue

Open Access Article. Published on 04 January 2021. Downloaded on 9/15/2024 1:15:01 AM.
This article is licensed under a Creative Commons Attribution 3.0 Unported Licence.

Check for updates

Cite this: *RSC Adv.*, 2021, **11**, 1200

# Tin dioxide-based nanomaterials as anodes for lithium-ion batteries

Minkang Wang,[a] Tianrui Chen,[b] Tianhao Liao,[a] Xinglong Zhang,[a] Bin Zhu,[a] Hui Tang *[a] and Changsong Dai *[b]

The development of new electrode materials for lithium-ion batteries (LIBs) has attracted significant attention because commercial anode materials in LIBs, like graphite, may not be able to meet the increasing energy demand of new electronic devices. Tin dioxide ($SnO_2$) is considered as a promising alternative to graphite due to its high specific capacity. However, the large volume changes of $SnO_2$ during the lithiation/delithiation process lead to capacity fading and poor cycling performance. In this review, we have summarized the synthesis of $SnO_2$-based nanomaterials with various structures and chemical compositions, and their electrochemical performance as LIB anodes. This review addresses pure $SnO_2$ nanomaterials, the composites of $SnO_2$ and carbonaceous materials, the composites of $SnO_2$ and transition metal oxides, and other hybrid $SnO_2$-based materials. By providing a discussion on the synthesis methods and electrochemistry of some representative $SnO_2$-based nanomaterials, we aim to demonstrate that electrochemical properties can be significantly improved by modifying chemical composition and morphology. By analyzing and summarizing the recent progress in $SnO_2$ anode materials, we hope to show that there is still a long way to go for $SnO_2$ to become a commercial LIB electrode and more research has to be focused on how to enhance the cycling stability.

Received 3rd December 2020
Accepted 21st December 2020

DOI: 10.1039/d0ra10194j

rsc.li/rsc-advances

## 1. Introduction

Lithium-ion batteries (LIBs) have been widely used in modern electronic equipment, such as laptops, mobile phones, and mechanical devices for their high energy densities, long cycle life, and environmental friendliness.[1–6] As an important component of LIBs, electrode materials are responsible for energy storage and cycling life of LIBs.[7–11] Currently, graphite is the main anode in commercial LIBs owing to its good stability.[12–14] However, it cannot fully meet the increasing energy demand for batteries due to its low theoretical specific capacity (372 mA h $g^{-1}$).[15–18] In order to solve this problem, much work has been focused on exploring alternative materials with high specific capacity.[19–26]

Potential candidates like metal oxides have been widely researched due to their high theoretical specific capacities, such as MnO,[27–30] $MnO_2$,[31–36] $Mn_3O_4$,[37–40] $Fe_2O_3$,[41–45] $Fe_3O_4$,[46–50] $Co_3O_4$,[51–54] and $SnO_2$.[55–57] Among these materials, $SnO_2$ has attracted significant attention due to its low cost, natural abundance, and high theoretical specific capacity (782 mA h $g^{-1}$ of bulk $SnO_2$). $SnO_2$ is superior to other metal oxides as it has a low charge and discharge potential, *i.e.*, an average charge and discharge potential of 0.5 V and 0.3 V *vs.* $Li/Li^+$, respectively,[58] resulting in LIBs with higher energy density. However, the commercial use of $SnO_2$ as an anode material is still hindered by poor cycling stability and inferior rate performance, which is attributed to the electrochemical reaction mechanism of $SnO_2$ during lithiation/delithiation. For $SnO_2$-based anode material for LIBs, the electrochemistry includes two steps, shown as follows:[59–61]

$$SnO_2 + 4Li^+ + 4e^- \rightarrow Sn + 2Li_2O \quad (1)$$

$$Sn + xLi^+ + xe^- \leftrightarrow Li_xSn\ (0 \leq x \leq 4.4) \quad (2)$$

In the first reaction, $SnO_2$ reacts with $Li^+$ and electrons to generate Sn and $Li_2O$. It is believed as an irreversible process, and this is the main reason why $SnO_2$ suffers severe capacity deterioration in the initial lithiation process.[62] In the second reaction, Sn obtained from the first step reacts with $Li^+$ and electrons to reversibly generate $Li_xSn$ alloys. The alloying and dealloying processes represent discharging and charging processes of $SnO_2$-based anode material, respectively.[63] However, Li-alloying anode materials like $Li_xSn$ and $Li_xSi$, possess the disadvantages of limited cycle life and severe capacity loss because of large volume changes, pulverization, and continuous formation of solid electrolyte interphase (SEI) during the alloying/dealloying process. Therefore, owing to this irreversible phase transformation process during lithiation/delithiation, the commercial use of $SnO_2$ is largely hampered.

[a]School of Materials and Energy, University of Electronic Science and Technology of China, Chengdu, 611731, China. E-mail: tanghui@uestc.edu.cn
[b]School of Chemistry and Chemical Engineering, Harbin Institute of Technology, Harbin 150001, P. R. China. E-mail: changsd@hit.edu.cn


© 2021 The Author(s). Published by the Royal Society of Chemistry

Open Access Article. Published on 04 January 2021. Downloaded on 9/15/2024 1:15:01 AM.
This article is licensed under a Creative Commons Attribution 3.0 Unported Licence.

In order to solve these problems and to improve the electrochemical performance of $SnO_2$, researchers have synthesized many $SnO_2$-based anode materials with various well-designed architectures. These $SnO_2$-based anode materials can be classified into four types, according to their chemical composition. The first category includes pure nanostructured $SnO_2$ materials, such as one-dimensional (1D) nanorods (NDs), nanotubes (NTs)[64–68] and nanowires (NWs),[69–74] two-dimensional nanobelts,[75,76] nanosheets[77–82] and nanoplates,[83–85] three-dimensional (3D) hollow nanostructures,[86–92] and hierarchical nanostructures.[93] Nanosized materials shorten transmission distance for electrons and $Li^+$ and also help to reduce the extent of volume changes during the electrochemical process. In addition, it has been reported that the reduction reaction of $SnO_2$ nanomaterials becomes reversible or partly reversible, which improves the lithium storage capacity and reduces the capacity loss during the charge/discharge process.[94] So the theoretic capacity of $SnO_2$ nanomaterials can be increased up to 1495 mA h $g^{-1}$. The second category includes the composites of $SnO_2$ and carbonaceous materials,[95–97] such as $SnO_2$/carbon nanotubes (CNTs),[98–101] $SnO_2$/hollow carbon spheres,[102–104] $SnO_2$/graphene[105–110] and $SnO_2$/amorphous carbon. Carbonaceous materials improve the conductivity of the composites and also provide abundant nanosized voids as buffers to decrease the effect of large volume changes during the charge/discharge process.[111–113] The third category includes the composites of $SnO_2$, transition metal oxides, and carbonaceous materials ($SnO_2$/TMOs/C). Various composites of $SnO_2$ and transition metal oxides ($SnO_2$/TMOs) have been synthesized in the past 20 years, such as $SnO_2/Fe_2O_3$,[114–117] $SnO_2/Co_3O_4$,[118,119] $SnO_2/TiO_2$,[120–122] $SnO_2$/ZnO[123] and $SnO_2/MoO_3$ (ref. 124) and they showed enhanced lithium storage capacity compared to pure $SnO_2$ anode material.[125] It has been reported that the introduction of TMOs, such as $Fe_2O_3$ (ref. 126) and $Co_3O_4$,[127] can effectively enhance the capacity because the transition metal nanoparticles in the composite can reversibly convert the extra $Li_2O$ into $Li^+$; thus, influencing the charge/discharge processes. However, cycling stability and rate performance of the composites still need to be further improved. Therefore, based on $SnO_2$/TMOs materials, much work has been done to

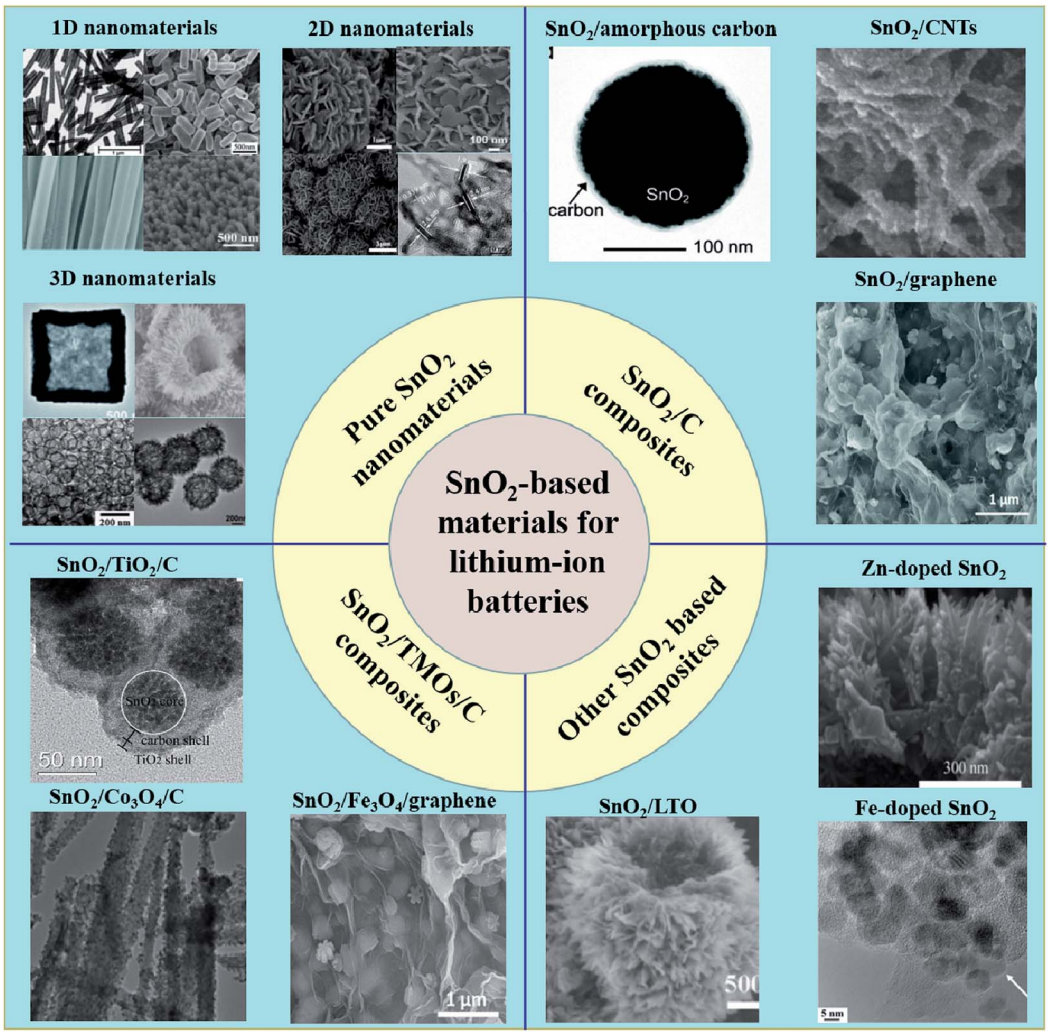


Scheme 1 Schematic presentation of different $SnO_2$-based anode materials for LIBs.

Open Access Article. Published on 04 January 2021. Downloaded on 9/15/2024 1:15:01 AM.
This article is licensed under a Creative Commons Attribution 3.0 Unported Licence.

synthesize the composites of $SnO_2$, TMOs, and carbonaceous materials ($SnO_2$/TMOs/C),[128–131] like $Fe_3O_4/SnO_2$/rGO,[132] $SnO_2$@C@$Fe_3O_4$ (ref. 133) and $SnO_2/MoO_3$/C.[134,135] $SnO_2$/TMOs/C materials more effectively alleviate the impact of volume changes and improve conductivity, leading to better electrochemical performance as an anode, compared to the $SnO_2$/TMOs materials.[136,137] The fourth category includes some other tin dioxide-based compounds, such as heteroatom-doped $SnO_2$ (ref. 138 and 139) (Fe-doped $SnO_2$,[140] Zn-doped $SnO_2$ (ref. 141)), $Li_4Ti_5O_{12}/SnO_2$ (ref. 142) and $SnO_2/C_3N_4$.[143]

In this article, we provide the recent progress in the research of these four major types of $SnO_2$-based anode material, as mentioned above (Scheme 1). For the following sections, we will introduce the various $SnO_2$-based nanomaterials as well as their corresponding synthesis methods and electrochemical performance. We hope this review article will serve as a good reference for further research.

## 2. Pure nanostructured $SnO_2$ materials

### 2.1 1D nanomaterials

Many 1D nanostructured $SnO_2$ materials, such as nanorods,[144–146] nanotubes[147–150] and nanowires[151–153] have been synthesized in recent years. 1D $SnO_2$ nanomaterials usually exhibit superior specific discharge capacity since they can offer extra channels and pathways for electron transmission compared to bulk $SnO_2$ and $SnO_2$ powders.[154–156]

**2.1.1 $SnO_2$ nanorods.** Pure $SnO_2$ nanorods can be synthesized *via* many methods such as chemical vapor deposition (CVD), vapor liquid solid,[157] hydrothermal treatment[158] and spray pyrolysis approach.[159] Among these reported methods, the hydrothermal synthesis of $SnO_2$ nanorods is the most used routine as it can be conveniently controlled due to its facile operation. The formation mechanism in a hydrothermal system can be summarized as follows:

$$Sn^{4+} + 4OH^- \rightarrow Sn(OH)_4 \rightarrow SnO_2 + 2H_2O \quad (3)$$

First, $Sn(OH)_4$ forms by the hydrolysis of Sn-based salts in aqueous medium. During the hydrothermal treatment, $Sn(OH)_4$ tends to convert into $SnO_2$ and subsequently grows along the [001] direction.[160,161] Early in 2003, Zhang *et al.* fabricated uniform $SnO_2$ nanorods with diameters of about 8–15 nm and lengths of about 150–200 nm by a one-step procedure under mild conditions.[148] They dissolved sodium dodecyl sulfate and $Sn(OH)_6^{2-}$ salt in a solution consisting of heptane and hexanol by stirring. Then, the homogeneously dispersed solution was transferred into a Teflon-lined autoclave and heated to 200 °C for 18 h. The as-prepared $SnO_2$ nanorods displayed a crystalline rutile structure. Zhang *et al.* also discovered that the concentration of $Sn(OH)_6^{2-}$ ions and the ratio of NaOH and $SnCl_4$ determined the shape of the $SnO_2$ nanorods. It was found that on increasing the concentration of $Sn(OH)_6^{2-}$ from 0.2 M to 0.3 M, the number of nanorods significantly decreased; additionally, on increasing the molar ratio of NaOH to $SnCl_4$ from 10 : 1 to 30 : 1, the aspect ratio of $SnO_2$ nanorods increased.[162]

In 2004, Cheng *et al.* investigated a large-scale hydrothermal method to synthesize single-crystalline $SnO_2$ nanorods with lengths of 15–20 nm and diameters of 2.5–5 nm (Fig. 1A). $Sn^{4+}$ precursor was dissolved in a mixture of water and alcohol, and pH was adjusted 12 and the solution was then heated at 150 °C for 24 h.[163] Based on Zhang and Cheng's work, many groups have synthesized $SnO_2$ nanorods *via* hydrothermal methods in other different systems. Guo *et al.* synthesized $SnO_2$ nanorods with diameter in the range of 120–260 nm and length up to 2–3 μm by using hexadecyltrimethylammonium bromide as a template (Fig. 1B).[58] Chen *et al.* synthesized single crystalline $SnO_2$ nanorods with diameters of 4–15 nm and lengths of 100–200 nm.[145] Xi *et al.* investigated a new synthesis method of ultrathin $SnO_2$ nanorods with an average diameter of 2 ± 0.5 nm.[164] Therefore, various $SnO_2$ nanorods with distinct morphology can be synthesized by controlling hydrothermal conditions.

$SnO_2$ nanorods can be applied as anode materials in LIBs.[165] Liu *et al.* synthesized $SnO_2$ nanorods arrays on a flexible alloy substrate *via* hydrothermal method. The nanorods arrays have average diameter and length of 60 and 670 nm, respectively (Fig. 1C). Observed by HRTEM images (Fig. 1D) and FFT pattern of HRTEM images (Fig. 1E), $SnO_2$ nanorod array was growing on substrate along [001] direction, since (001) plane is more loosely packed and has a relatively high surface energy compared to {110} planes.[166] As-collected hierarchical array structure can directly be used as a binder-free electrode for LIBs, which shows good energy performance, including high discharge capacity

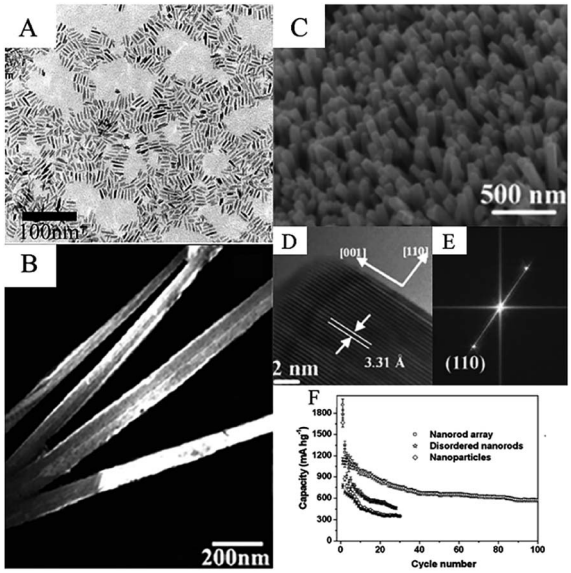


Fig. 1 (A) Transmission electron microscopy (TEM) images of the as-prepared $SnO_2$ nanorods (adapted with permission from ref. 163 copyright 2004 American Chemical Society). (B) Scanning electron microscopy (SEM) images of long $SnO_2$ nanorods (adapted with permission from ref. 58 copyright 2004 Elsevier). (C) SEM images, (D) high-resolution TEM (HRTEM) images, (E) FFT patterns of the HRTEM images, and (F) cycling performance of $SnO_2$ nanorods (adapted with permission from ref. 154 copyright 2009 Royal Society of Chemistry).

 © 2021 The Author(s). Published by the Royal Society of Chemistry

Open Access Article. Published on 04 January 2021. Downloaded on 9/15/2024 1:15:01 AM.
This article is licensed under a Creative Commons Attribution 3.0 Unported Licence.

(the first discharge is 1918 mA h $g^{-1}$) and good cycling stability (580 mA h $g^{-1}$ after 100 cycles at 0.1C, with coulombic efficiency of nearly 100%) (Fig. 1F).[154]

**2.1.2 $SnO_2$ nanotubes.** $SnO_2$ nanotubes have been widely used as anode materials in lithium-ion batteries. Compared to $SnO_2$ nanorods, $SnO_2$ nanotubes usually possess superior lithium storage capacity and cycling stability due to their hollow characteristics.[167] Sacrificial template-based approaches are commonly used in synthesizing this tubular structure. Anodic aluminum anode (AAO), polycarbonate (PC) membrane, $SiO_2$ and ZnO can be served as sacrificial templates in synthesizing metal oxides nanostructures. The synthesis process of $SnO_2$ nanotubes usually includes three steps: (1) infiltration of reactants into the templates; (2) growth of $SnO_2$ with designed shapes and morphology; (3) removal of the template.

Early in 2006, Lai *et al.* reported the preparation of $SnO_2$ nanotubes with a thickness of 10 nm and a length of about 0.4–1.4 μm *via* the electrodeposition method (Fig. 2A). They first electroplated the $SnO_2$ nanoparticles on a gold electrode which was modified with a porous PC membrane. Then, the $SnO_2$ particles were annealed at 650 °C in ambient conditions. The shape and size of the as-prepared nanotubes could be easily controlled by monitoring the charge passed.[66] Meanwhile, Lai *et al.* also reported that the $SnO_2$ nanotubes possessed better crystallinity and uniformity in terms of length and width.

The AAO and PC membrane-template methods have been widely used in the synthesis of metal oxide nanotubes. Wang *et al.* fabricated uniform polycrystalline $SnO_2$ nanotubes *via* this template.[68] They found that the diameter, thickness, length, and texture of nanotubes can be controlled with template structure, pristine particle size, and heating-rate temperature. As shown in Fig. 2B–D, nanotube walls, with a thickness of about 10–25 nm, were composed of abundant nanocrystallites of 6–15 nm. Furthermore, the $SnO_2$ nanotube electrode showed superior charge/discharge performance compared to $SnO_2$ nanoparticles. The specific capacity of the $SnO_2$ nanotube electrode can be 525 mA h $g^{-1}$ after 80 cycles.[68] They summarized that the improved cycling performance resulted from the following factors, (1) cavities in the nanotubes which provide space and reduce the effect of volume change during lithiation/delithiation process; (2) $SnO_2$ nanotubes provide more active sites for $Li^+$ intercalation and deintercalation; and (3) compared to $SnO_2$ nanoparticles, the $SnO_2$ nanotubes are less movable and result in less agglomeration.[68] Si and $SiO_2$ have been commonly used in the synthesis of hollow nanostructures, including nanotubes. Morphology and shapes of $SnO_2$ nanotubes can be well designed by controlling the shape of the Si templates and the hydrothermal conditions.[168] Ye *et al.* also discovered that the shorter $SnO_2$ nanotubes showed superior electrochemical performance, since the hollow structure in the short nanotubes can alleviate the volume changes.[147] ZnO is another promising sacrificial template used for synthesizing $SnO_2$ nanotube arrays as ZnO can be conveniently synthesized and removed. The as-prepared nanotubes exhibited a diameter and thickness of about 100–300 nm and about 10–20 nm, respectively, composed of nanoparticles with diameters of about 2–5 nm (Fig. 2E and F). The material also showed high capacity and improved cycling performance, *i.e.*, 750–800 mA h $g^{-1}$ after 20 cycles at 0.1C, as shown in Fig. 2G.[64]

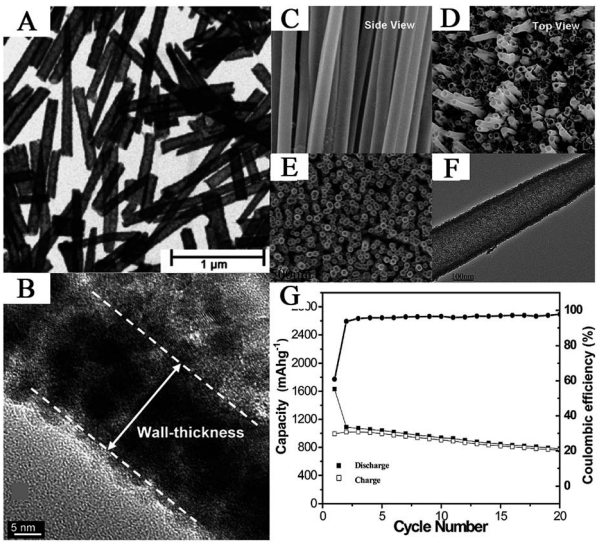


Fig. 2 (A) TEM image of $SnO_2$ nanotubes (adapted with permission from ref. 66 copyright 2006 Royal Society of Chemistry). (B) HRTEM image of $SnO_2$ nanotubes for measuring thickness, (C) FESEM image of the side view, and (D) FESEM images of the top view of $SnO_2$ nanotubes (adapted with permission from ref. 68 copyright 2005 American Chemical Society). (E) TEM image, (F) HRTEM image, and (G) discharge capacity *vs.* cycle number of $SnO_2$ nanotube arrays on Ti substrates (adapted with permission from ref. 64 copyright 2011 American Chemical Society).

**2.1.3 $SnO_2$ nanowires.** Template-based methods have also been widely used to synthesize $SnO_2$ nanowires. These sacrificial templates contribute to the development of mesoporous and hollow $SnO_2$ nanowires.[63,169] Kim *et al.* fabricated a $SnO_2$ nanowire-based anode material for LIBs by using KIT-6 and SBA-15 $SiO_2$ as hard templates. They first dissolved $SnCl_4 \cdot 5H_2O$ and the hard templates in DI water and stirred the mixture at room temperature until $Sn^{4+}$ was adsorbed by templates. Then, the resulting composites were annealed, and the templates were removed from the composites using a NaOH solution. The as-obtained $SnO_2$ nanowires had a diameter of 6 nm and a length greater than 3 μm, and the size of mesoporous $SnO_2$ on the surface of the nanowire was 3.8 nm with a BET surface area of 160 $m^2$ $g^{-1}$. Such a porous and interconnected $SnO_2$ nanowire structure showed better lithium storage capacity. The initial discharge and charge capacities of the nanowire anode were 1595 and 800 mA h $g^{-1}$ at 0.2C, respectively, and the discharge capacity remained at 773 mA h $g^{-1}$ after 50 cycles. These observations can be attributed to the mesopores which act as a buffer zone against $SnO_2$ volume expansion.[71]

Researchers have synthesized $SnO_2$ nanowires *via* many methods. For example, Ko *et al.* synthesized $SnO_2$ nanowires on the current collector *via* thermal evaporation at (600 °C). The as-prepared $SnO_2$ nanowires exhibited a highly-ordered single-crystalline phase with a thin diameter of 40–50 nm and length of more than 1 μm (Fig. 3A and B). The $SnO_2$ nanowire-based anode exhibited high specific discharge capacity and good

Open Access Article. Published on 04 January 2021. Downloaded on 9/15/2024 1:15:01 AM.
This article is licensed under a Creative Commons Attribution 3.0 Unported Licence.

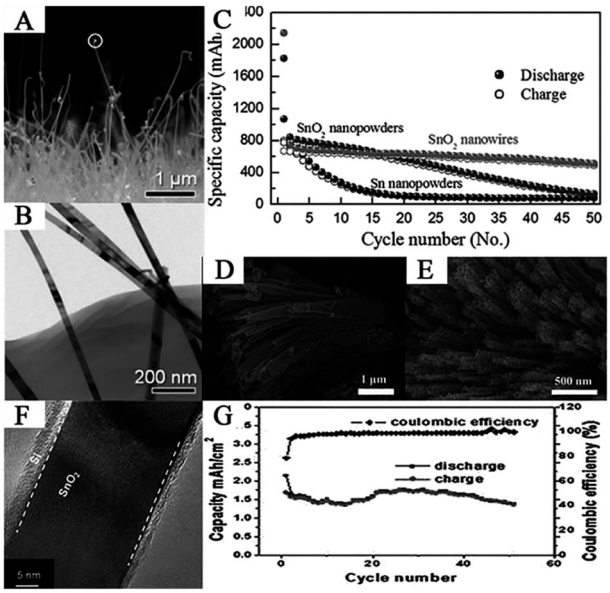


Fig. 3 (A) Cross-sectional FESEM image, (B) TEM image, and (C) comparative cycling performance of the $SnO_2$ nanowires (adapted with permission from ref. 72 copyright 2009 IOP Publishing). (D and E) SEM images of $SnO_2$ porous nanowire bundles (adapted with permission from ref. 170 copyright 2011 Royal Society of Chemistry). (F) HRTEM image, and (G) cycling performance of the $SnO_2$@Si nanowires (adapted with permission from ref. 73 copyright 2013 Royal Society of Chemistry).

cycling performance, *i.e.*, 2140 mA h $g^{-1}$ at the first cycle and 510 mA h $g^{-1}$ at the 50$^{th}$ cycle at 1C (Fig. 3C).[72] Ding *et al.* reported a facile strategy for the synthesis of $SnO_2$ nanowire arrays using SBA-15 nanorods as a template by infiltrating molten $SnCl_2$ into the channels of the SBA-15 nanorods followed by calcination and removal of the template.[69] Han *et al.* investigated the synthesis of porous $SnO_2$ nanowire bundles with a high yield *via* solution-based approaches. This hierarchical nanostructure is made up of $SnO_2$ nanowires with an overall diameter of 80–120 nm and an average length of 6 μm (Fig. 3D). Moreover, the as-prepared nanowires have a highly porous structure composed of numerous nanocrystals.[170] Ren *et al.* synthesized 3D hierarchical $SnO_2$ nanowire arrays on carbon cloth by first, a CVD method for $SnO_2$ nanowires, followed by a Plasma Enhanced-CVD (PECVD) method for Si thin film coating. The $SnO_2$@Si nanowire arrays can directly serve as a flexible and binder-free anode for LIBs. In this unique structure, $SnO_2$ nanowires act as a lithium storage material and a conductive matrix to support Si; in addition, the thin Si layer acts as a buffer for $SnO_2$ to reduce the effect of volume changes (Fig. 3F). Anodes based on such novel hierarchical structures showed excellent electrochemical performance with discharge capacity of 2.13 mA h $cm^{-2}$ in the first cycle and 1.386 mA h $cm^{-2}$ after 50 cycles, *i.e.*, 65% of the first cycle (Fig. 3G).[73] Thus, in this section, different synthesis methods for $SnO_2$ nanowires, corresponding morphologies, and electrochemical properties have been presented, demonstrating that $SnO_2$ nanowires are promising anode materials for LIBs.

### 2.2 2D nanomaterials

Due to the difficulty of synthesizing well-defined 2D $SnO_2$ nanomaterials, obtaining a large variety of 2D $SnO_2$ nanostructures is significantly harder than 1D and 3D nanomaterials. The anisotropic crystal growth of $SnO_2$, in the formation process, limits the synthesis of 2D nanomaterials.[82] In order to overcome this problem, *in situ* growth of $SnO_2$ nanosheets on physical or chemical substrates has been widely investigated.[171,172] Among these fabrication processes, $SnO_2$ nanosheets grown on physical substrates, such as metal foam,[49,173–175] foil,[77,154,176–178] carbon cloth[78,179] and graphite paper[180–183] can be directly used as binder-free and current-collector free electrode in LIBs due to excellent conductive and supportive properties of such substrates. Meanwhile, some organic macromolecules can be used as chemical templates to fabricate $SnO_2$ nanosheets. These substrates could provide a growth plane for $SnO_2$ nanosheets and inhibit self-aggregation during the lithiation/delithiation processes.[184] Moreover, $SnO_2$ nanosheets have a tendency to assemble into complex structures, such as nanosheet arrays, clusters, and spheres, which usually exhibit superior lithium storage capacities due to their highly interconnected and hierarchical nanostructures.[184–187]

Zhao *et al.* fabricated $SnO_2$ nanosheet arrays on Ni foam with a thickness of 20 nm and a length of 500 nm (Fig. 4A) *via* a hydrothermal method. Nickel foam, *i.e.*, a 3D macroporous conductive network, was used as a supportive substrate to fabricate $SnO_2$ nanosheet arrays, which can be directly used as a binder-free anode in LIBs. Due to the high electroactive surface area, ultrathin sheets, and shorter electron transport pathways, the nanosheets exhibited excellent electrochemical properties. The novel anode showed an initial discharge capacity of approximately 1800 mA h $g^{-1}$ and remained at 674.9 mA h $g^{-1}$ after 50 cycles at 0.5C (Fig. 4B).[79] Moreover,

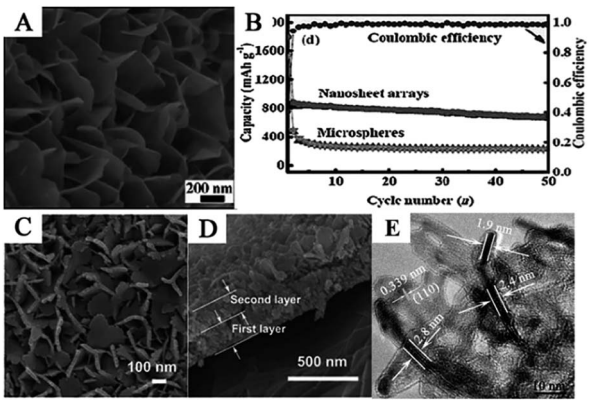


Fig. 4 (A) SEM image, and (B) cycling performance of hierarchical $SnO_2$ nanosheet arrays on nickel foam (adapted with permission from ref. 79 copyright 2014 Wiley). (C) Top view, and (D) cross-sectional FESEM images of $SnO_2$ nanosheets double layer on Ti foil (adapted with permission from ref. 77 copyright 2014 Royal Society of Chemistry). (E) HRTEM image of ultrathin $SnO_2$ nanosheets of less than 5 nm (adapted the permission from ref. 80 copyright 2015 American Chemical Society).

 © 2021 The Author(s). Published by the Royal Society of Chemistry

Open Access Article. Published on 04 January 2021. Downloaded on 9/15/2024 1:15:01 AM.
This article is licensed under a Creative Commons Attribution 3.0 Unported Licence.

interconnected single and double layer $SnO_2$ nanosheets were also fabricated on three different conductive substrates, *i.e.*, Ti, Cu foil, and flexible graphite paper, as integrated binder-free electrodes for LIBs. The nanosheets were interconnected with each other to form a hierarchical network, and the thickness of a single $SnO_2$ nanosheet layer was about 250 nm (Fig. 4C and D). The electrodes delivered high specific capacity, excellent cycling stability, and good rate capability.[77,79] Zhu *et al.* reported an ultra-rapid, low-cost, and simple microwave-assisted synthesis of ultrathin $SnO_2$ nanosheets with a thickness of less than 5 nm (Fig. 4E). The ultrathin $SnO_2$ nanosheets exhibited significantly enhanced electrochemical lithium storage properties with a high reversible capacity of 757.6 mA h $g^{-1}$ at a current density of 200 mA $g^{-1}$ up to 40 cycles. The ultrathin 2D nanosheets can significantly reduce the ion diffusion paths and allow faster phase transitions; furthermore, the sufficient external surface interspace and porous configuration successfully accommodate the large volume changes.[77,78,80]

Many complex hierarchical $SnO_2$ nanostructures were also assembled by 2D $SnO_2$ nanosheets. Flower-like $SnO_2$ assembled by many $SnO_2$ nanosheets, with an average thickness of 100 nm, have been synthesized on a flexible carbon cloth using CVD at 750 °C.[78] SEM images (Fig. 5A) show that as-prepared flower-like $SnO_2$ nanostructures were formed by an assembly of numerous nanosheets with a thickness of 100 nm. Ding *et al.* synthesized hollow spheres assembled from $SnO_2$ nanosheets (Fig. 5B), using sulfonated polystyrene hollow spheres (sPSHSs) as a template; the surface of the sPSHS is covered with $-SO_3-$ functional groups. Therefore, the $Sn^{2+}$ ions can easily interact with these templates *via* electrostatic forces and subsequently grow into $SnO_2$ nanosheets, assisted by mercaptoacetic acid. Moreover, sPSHSs templates are beneficial for minimizing the gas outflux during the template removal process, which helps the retention of the final structure.[188–191] The as-prepared samples showed a superior cycling capacity retention compared to other $SnO_2$ nanoflowers assembled by $SnO_2$ nanosheets as well as $SnO_2$ nanoparticles, indicating the positive effect of the unique nanostructure (Fig. 5C).[87] Wei *et al.* fabricated nanoporous $SnO_2$ nanosheets *via* a simple one-step ultrasonic-assisted chemical precipitation strategy with polyvinylpyrrolidone (PVP) as a soft template. Due to the porous nanosheet structure, it exhibited high capacity, *i.e.*, an initial discharge capacity of 2231 mA h $g^{-1}$ at 0.2 A $g^{-1}$, and excellent cycling performance, *i.e.*, an initial discharge capacity of 710 mA h $g^{-1}$ and 606 mA $g^{-1}$ at 1.6 A $g^{-1}$ and 4 A $g^{-1}$, respectively, which remained at 497 mA h $g^{-1}$ and 280 mA h $g^{-1}$ after 60 cycles, respectively (Fig. 5D).[81]

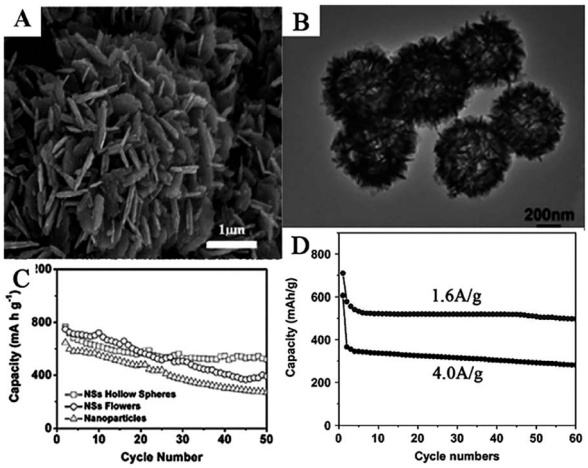


Fig. 5 (A) SEM images of flower-like $SnO_2$ nanosheets (adapted with permission from ref. 78 copyright 2014 Elsevier). (B) TEM image, and (C) cycling performance of $SnO_2$ nanosheets hollow spheres (adapted the permission from ref. 87 copyright 2011 Royal Society of Chemistry). (D) Cycling performance of $SnO_2$ nanosheets at 1.6 A $g^{-1}$ and 4.0 A $g^{-1}$ (adapted the permission from ref. 81 copyright 2017 Elsevier).

### 2.3 3D nanomaterials

In recent years, 3D $SnO_2$ structures have attracted significant attention.[86] Various 3D nanostructures have been synthesized, such as hollow spheres[91,192–194] and microboxes.[195–197] Furthermore, many new synthetic methods to prepare $SnO_2$ hollow structures, including Ostwald ripening,[198–200] Kirkendall effect,[201–204] removable templates[195] and chemically induced self-assembly[192,205] have been reported.

In 2006, Lou *et al.* investigated a one-pot template-free synthesis of hollow $SnO_2$ nanostructures, based on an unusual inside-out Ostwald ripening mechanism. The synthesis process was performed in an ethanol–water (EtOH–$H_2O$) mixed solvent with $K_2SnO_3$ as the precursor, followed by a hydrothermal treatment. Lou *et al.* discovered that the concentration of the precursor and the ratio of EtOH in the mixed solvent determined both the particle size and morphology of the product. Moreover, the addition of urea or thiourea in the synthetic mixtures was also found to increase the product yield, morphological yield to nearly 100%, and a well-dispersed monodispersity (Fig. 6A–C). Such hollow $SnO_2$ nanosphere-based anode material exhibited high discharge capacity and good cycling performance, *i.e.*, an initial discharge capacity of 1140 mA h $g^{-1}$, which is comparable to the theoretical capacity of graphite after more than 40 cycles.[86]

Porous hollow $SnO_2$ micro-boxes have been synthesized *via* a selective leaching strategy using $ZnSn(OH)_6$ as the precursor. $ZnSn(OH)_6$ micro-boxes were first formed through a modified one-pot co-precipitation method and subsequently, the Zn species were removed *via* a selective leaching strategy. The TEM image (Fig. 6D) shows that the thickness of the shell was about 100 nm.[195] Hu *et al.* used a template-and additive-free hydrothermal route to prepare a uniquely shaped $SnO_2$ material that comprised of a hollow spherical morphology with uniform diameter and very thin petal-like nanosheets grown perpendicularly on the surface of the spheres, resembling a "chestnut cupule" (Fig. 6E). In contrast to conventional $SnO_2$ materials, this unique morphology significantly improved the storage capacity and cycling performance of $SnO_2$ as an anode material for lithium and sodium ion batteries.[206]

In addition, 3D hierarchical $SnO_2$ nanomaterials can be assembled by 0D, 1D, and 2D $SnO_2$ nanomaterials. For example, 0D crystalline $SnO_2$ nanoparticles were successfully assembled

Open Access Article. Published on 04 January 2021. Downloaded on 9/15/2024 1:15:01 AM.
This article is licensed under a Creative Commons Attribution 3.0 Unported Licence.

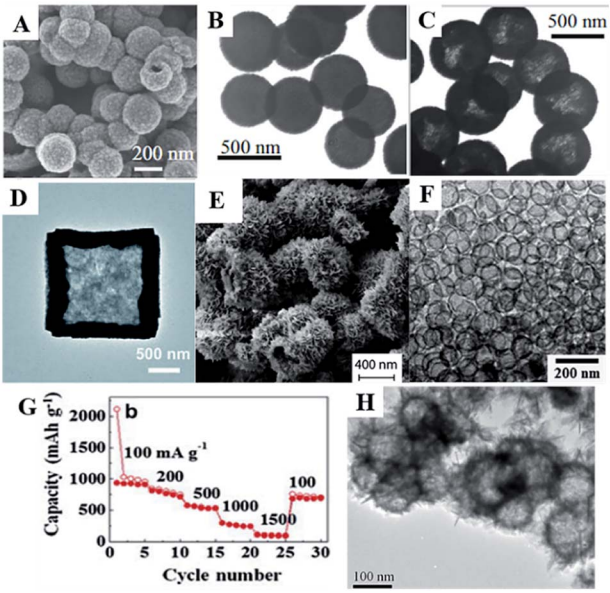


Fig. 6 (A) FESEM images of $SnO_2$ hollow nanosphere prepared in the solvent of EtOH : $H_2O$ ratio of 1 : 1. (B) TEM images of $SnO_2$ hollow nanosphere prepared with the value of EtOH in the solvent of EtOH–$H_2O$ = 37.5%. (C) TEM images of $SnO_2$ hollow nanosphere prepared with the value of EtOH in the solvent EtOH–$H_2O$ = 37.5% and 0.1 M urea (adapted the permission from ref. 86 copyright 2006 WILEY). (D) TEM images of $SnO_2$ microboxes (adapted the permission from ref. 195 copyright 2016 Royal Society of Chemistry). (E) SEM images of $SnO_2$ hierarchical hollow microspheres (adapted the permission from ref. 205 copyright 2017 Royal Society of Chemistry). (F) TEM images, and (G) rate performance of $SnO_2$ hollow spheres (adapted with permission from ref. 91 copyright 2012 Elsevier). (H) TEM image of the hierarchical $SnO_2$ (adapted with permission from ref. 210 copyright 2010 American Chemical Society).

into a high-order nanostructure of hollow core–shell. First, $SnCl_4$ was dissolved in a mixture of DI water and ethanol to form a homogeneous solution which was heated to 180 °C for 24 h. Then, the collected sediments were calcined in air to remove carbon by oxidation. FESEM showed that the mesospheres had an overall dimension of 1–3 μm, and the surface of the spheres was formed by small aggregated $SnO_2$ nanoparticles (11 nm). The shell was estimated to be approximately 200 nm in thickness. This unique $SnO_2$ nanostructure could store an exceedingly large amount of $Li^+$ and cycled well for a pure phase $SnO_2$ anode.[207–209] Hollow urchin-like $SnO_2$ nanospheres have been fabricated using ultrathin nanorods *via* a solvothermal route. The diameters of urchin-like nanospheres and nanorods are about 300 and 100 nm, respectively. The as-obtained hollow urchin-like $SnO_2$ nanospheres with ultrathin 1D nanorods exhibited high capacity and excellent rate discharging performance. The 1st, 2nd, 20th, and 50th discharge capacities were 1881 mA h $g^{-1}$, 1090 mA h $g^{-1}$, 781 mA h $g^{-1}$, and 719 mA h $g^{-1}$, respectively, at a current density of 100 mA $g^{-1}$. Upon changing the discharge–charge rates to 0.2, 0.4, 0.8, 1, 2, and 0.4C, the capacities of urchin-like $SnO_2$ were maintained at 815, 687, 601, 446, 282, and 520 mA h $g^{-1}$, respectively, while for commercial $SnO_2$, the capacities were only 828, 677, 512, 386, 246, 133, and 375 mA h $g^{-1}$, respectively. The retention of the reversible capacity of the hollow nanosphere electrodes was better than that of commercial $SnO_2$ samples.[210] Furthermore, $SnO_2$ hollow nanospheres can also be synthesized by sol–gel methods.[91] The size of the hollow spheres is controlled by using different-sized templates. As-prepared $SnO_2$ shells are almost amorphous and exhibit a rutile phase after annealing at 600 °C. The size of the $SnO_2$ hollow spheres ranges from 25 to 100 nm (Fig. 6F), and the thickness of the shell is constantly 5 nm despite the size of the hollow spheres. Due to the nanosized hollow sphere and thin shell thickness, $SnO_2$ hollow spheres show excellent electrochemical performance. The smallest hollow sphere of $SnO_2$ (25 nm) exhibited a high reversible capacity of 750 mA h $g^{-1}$ as well as good rate performance, *i.e.*, 700 mA h $g^{-1}$ at 0.2 A $g^{-1}$ and 530 mA h $g^{-1}$ at 0.5 A $g^{-1}$ (Fig. 6G).[91] Hierarchical $SnO_2$ hollow nanostructures can also be assembled by 2D nanosheets. As shown in Fig. 6H, the hierarchical $SnO_2$ shows high capacities and excellent cycle performance as an anode material for LIBs. The improved electrochemical properties could be ascribed to the large surface area, enhanced structure stability, and short diffusion length for both lithium ions and electrons.[211]

## 3. Composites of $SnO_2$ and carbonaceous materials

### 3.1 $SnO_2$ with carbon nanotubes (CNTs)

Nanocomposites of $SnO_2$ and CNTs reportedly exhibit improved lithium storage capacities compared to pure $SnO_2$ materials.[212] This can be attributed to the flexible nature and superior conductivity of the CNTs, which alleviates the internal stress caused during the charge/discharge process[213–215] and enhances the electron transportation. With increased conductivity and surface area, such nanocomposites show enhanced lithium storage capability.[216,217]

Wen *et al.* reported an *in situ* synthesis of mesoporous $SnO_2$ on the surface of multi-walled CNTs (MWCNTs) through a hydrothermal method utilizing CTAB as the structure-directing agent. The MWCNTs/$SnO_2$ hybrid electrodes showed great electrochemical performance and cycling stability. This can be attributed to the synergistic effects of the unique combination of properties including their one-dimensional hollow structure, high-strength with flexibility, excellent electric conductivity, and large surface area, which helped alleviate the effect of volume expansion, shorten the distance of $Li^+$ diffusion, and contribute to the transmission of electrons.[100,218–221]

In another hydrothermal system, Du *et al.* synthesized $SnO_2$/MWCNT composites by a simple solvothermal method and subsequent heat treatment at 360 °C with $SnCl_2$ and CNTs as reactants. The distribution of $SnO_2$ nanocrystals can be controlled by changing the molar ratio of $Sn^{2+}$ and CNTs in the precursor. For $SnO_2$/MWCNTs composites prepared with a molar ratio of Sn : C = 0.3 : 1, a uniform layer of $SnO_2$ nanocrystals, with a crystal size of about 5 nm, was deposited on the surface of the MWCNTs (Fig. 7A).[222] These composites showed

 © 2021 The Author(s). Published by the Royal Society of Chemistry

Open Access Article. Published on 04 January 2021. Downloaded on 9/15/2024 1:15:01 AM.
This article is licensed under a Creative Commons Attribution 3.0 Unported Licence.

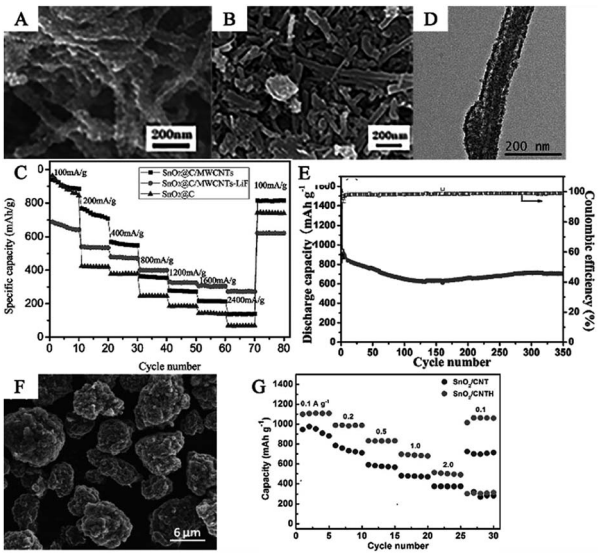


Fig. 7 (A) FESEM image of $SnO_2$/CNT composites prepared with MSn : C = 0.3 : 1 (adapted with permission from ref. 221 copyright 2009 Elsevier). (B) SEM image, and (C) rate performance of $SnO_2$@C/MWCNTs-LiF (adapted with permission from ref. 224 copyright 2019 Elsevier). (D) TEM image and (E) cycling performance of CNT@void@$SnO_2$@C composite (adapted the permission from ref. 225 copyright 2015 Elsevier). (F) SEM image, and (G) rate performance of $SnO_2$/CNTH composites (adapted with permission from ref. 226 copyright 2019 American Chemical Society).

very stable cycling retention, of up to 100 cycles, because of nanosized materials and the introduction of CNTs.[201,223] Jin *et al.* prepared $SnO_2$/MWCNTs electrodes *via* a hydrothermal method at 150 °C for 24 h. The $SnO_2$ nanoparticles with diameters of less than 3 nm were uniformly loaded onto the surface of MWCNTs. The MWCNT/$SnO_2$ nanocomposites exhibited a high reversible capacity of 420 mA h $g^{-1}$ even after 100 cycles.[137,224]

In order to further improve electrochemical properties of the $SnO_2$/CNTs hybrid nanomaterials, many groups have synthesized various $SnO_2$/CNTs-based anode materials. For example, Liang *et al.* synthesized $SnO_2$@C/MWCNTs-lithium fluoride (LiF) composite nanomaterials (Fig. 7B). Carbon-coated $SnO_2$ ($SnO_2$@C) was prepared by a spray drying method, with water-soluble asphalt as the carbon source and MWCNTs as the conductive agent. The conductivity was significantly enhanced, and the extent of volume expansion of the $SnO_2$ was reduced. Compared to $SnO_2$/CNTs, the presence of LiF enhanced the stability of the SEI film and improved the coulombic efficiency and capacity retention rate of the electrode. After 200 cycles, the $SnO_2$@C/MWCNTs-LiF anode still maintained 70.1% of the capacity retention rate and the specific capacity was held at 274 mA h $g^{-1}$ at 2400 mA $g^{-1}$, compared with 136 mA h $g^{-1}$ for the $SnO_2$@C/MWCNTs anode (Fig. 7C).[225] Tian *et al.* fabricated a tube-in-tube nanostructure, denoted as CNT@void@$SnO_2$@C, by a facile hydrothermal method and subsequent carbonation with polysaccharide as the carbon source, $SiO_2$ as the sacrificial template, and $NH_4F$ as the etchant. The CNT@void@$SnO_2$@C exhibited one-dimensional nanostructures with average diameters of about 100–150 nm and hollow structures filled with abundant voids (Fig. 7D). Tian *et al.* interpreted the formation mechanism as follows: (1) the crystallization and deposition of $SnO_2$ could occur prior to the polycondensation of glucose; (2) the formation rate of $SnO_2$@polysaccharide was faster than the etching rate of $SiO_2$ by $NH_4F$ due to the slow etching process of $SiO_2$ by $NH_4F$ solution under hydrothermal condition; and (3) the large void-space between the $SnO_2$@-polysaccharide and CNT, formed after the $SiO_2$ coating layer, was etched away completely. The CNT@void@$SnO_2$@C exhibited good electrochemical properties, delivering a reversible capacity of 702.5 mA h $g^{-1}$ at 200 mA $g^{-1}$ even after 350 cycles (Fig. 7E). This indicated that the unique tube-in-tube nanostructure, as well as the one-dimensional void space, which formed between the inner CNT and outer $SnO_2$@C nanotubes, contributed significantly to the electrochemical performance.[226] Liu *et al.* synthesized ultrafine $SnO_2$ (6–7 nm)/carbon nanotube hairball ($SnO_2$/CNTH) composites with a 3D hierarchical structure (Fig. 7F), which was prepared by spray drying and a solvothermal method. Fig. 7G shows that $SnO_2$/CNTH exhibited superior electrochemical performance and improved the lithium storage capacity compared to conventional $SnO_2$/CNT. The improved electrochemical performance can be attributed to the increased conductivity and enhanced electrode reactivity due to the 3D hierarchical cross-linked structure. This structure can also address the large volume changes upon cycling.[227]

### 3.2 $SnO_2$ with amorphous carbon

Hydrothermal treatment followed by carbonization is the most common method for synthesizing $SnO_2$/amorphous carbon nanomaterials.[228–230] There are mainly two synthesis routes of $SnO_2$/amorphous carbon; one is to treat $Sn^{2+}$ or $Sn^{4+}$ salt with the precursor of carbon,[231–236] and the other is to deposit a carbon layer on the as-prepared $SnO_2$ nanostructures.[237,238] Conventional amorphous carbon can be derived from glucose,[239,240] sucrose[241,242] and many organic compounds.[243] The morphology and shapes of the nanostructures can be adjusted by the hydrothermal and annealing conditions.

Various $SnO_2$/C nanomaterials have been synthesized in recent years, such as carbon-coated $SnO_2$ NPs,[244–247] carbon-coated $SnO_2$ nanorods,[248,249] carbon-coated $SnO_2$ nanowires[151,217] and carbon-coated $SnO_2$ nanotubes.[57] Different structures and morphologies of $SnO_2$ are known to lead to different electrochemical performance. In 2008, Lou *et al.* prepared $SnO_2$/C composite hollow spheres. The mesoporous $SnO_2$ hollow spheres were embedded in 3D carbon networks (Fig. 8A). The carbon networks act as a physical buffering cushion for the intrinsic large volume change and electronically conducting pathways. Compared to $SnO_2$ hollow spheres and graphite, these $SnO_2$/carbon hollow spheres were able to deliver a reversible lithium storage capacity of 473 mA h $g^{-1}$ after 50 cycles (Fig. 8B).[99] In 2009, Lou *et al.* also synthesized a thin layer of carbon-coated $SnO_2$ nano-colloids (Fig. 8C) and coaxial $SnO_2$@carbon hollow nanospheres (Fig. 8D) by a simple hydrothermal method followed by carbonization; both

Open Access Article. Published on 04 January 2021. Downloaded on 9/15/2024 1:15:01 AM.
This article is licensed under a Creative Commons Attribution 3.0 Unported Licence.

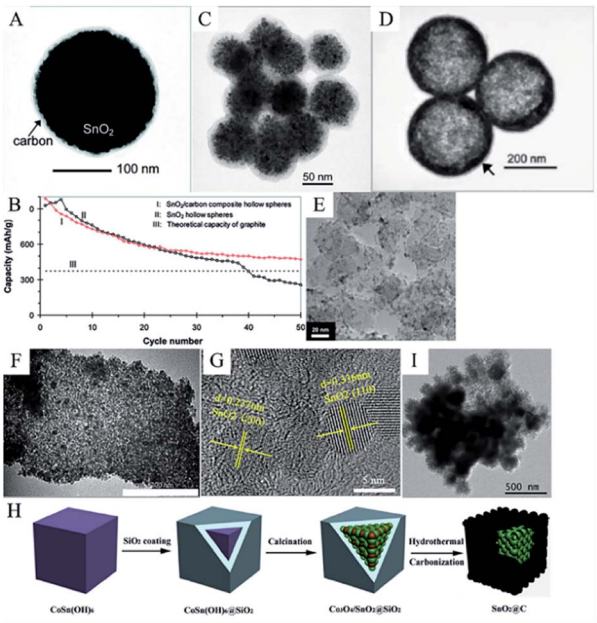


Fig. 8 (A) TEM image, and (B) cycling performance of $SnO_2$/carbon composites hollow spheres (adapted with permission from ref. 99 copyright 2008 American Chemistry Society). (C) TEM image of carbon-coated $SnO_2$ nanocolloids obtained after carbonization at 550 °C (adapted with permission from ref. 239 copyright 2009 American Chemical Society). (D) TEM image of $SnO_2$@carbon hollow nanospheres (adapted with permission from ref. 240 copyright 2009 Wiley). (E) TEM image of nanosized $SnO_2$/carbon composites (adapted with permission from ref. 248 copyright 2009 Elsevier). (F) TEM image, and (G) HRETM image of $SnO_2$/RHPC composite materials (adapted with permission from ref. 231 copyright 2019 Elsevier). (H) The fabrication schematic of $SnO_2$@non-smooth carbon. (I) TEM image of $SnO_2$ quasi-nanocubes@non-smooth carbon (adapted with permission from ref. 255 copyright 2019 Elsevier).

exhibited improved electrochemical performance.[57,250] Courtel *et al.* reported an *in situ* synthesis of $SnO_2$ nanoparticles (5–10 nm)/carbon composite materials using the polyol method by oxidizing $SnCl_2 \cdot 2H_2O$ in the presence of a carbon matrix. The TEM image (Fig. 8E) show that the $SnO_2$ nanoparticles were uniformly embedded in the carbon matrix. Based on the nanostructure, the as-obtained composites showed an improved lithium storage capacity of 370 mA h $g^{-1}$ at 200 mA $g^{-1}$ and a lower capacity fading compared to commercial $SnO_2$ (50 nm).[251]

While the morphology and structure of $SnO_2$ influence the electrochemical properties of the $SnO_2$/C composites, different carbonaceous materials also influence the performance of the composite. Xu *et al.* prepared composites of $SnO_2$/ordered mesoporous carbon ($SnO_2$/OMC) through a hydrolysis process. OMC, a novel kind of carbon material, has been widely used in LIBs due to its large surface area, high conductivity, and highly porous structure; it promotes the diffusion of lithium ions and electrolyte. The $SnO_2$/OMC composites delivered a good cycling performance with a reversible capacity of 395.6 mA h $g^{-1}$ for up to 50 cycles.[252] Shi *et al.* synthesized $SnO_2$/rice-husk-based porous carbon composites (RHPC) *via* a simple melt-impregnation method with a heat treatment route. RHPC can be easily and cheaply obtained by convenient carbonization and activation of rice husk. The TEM images (Fig. 8F and G) show that the $SnO_2$ nanoparticles with the average size of 4 nm can be loaded on the RHPC matrix. The cycling measurements showed that the discharge capacity of the RHPC/$SnO_2$ anode at the current density of 100 mA $g^{-1}$, at the 50$^{th}$ cycle, was 550 mA h $g^{-1}$, which demonstrated that in contrast to pure $SnO_2$ anodes, the cycling performance of the RHPC/$SnO_2$ anode was remarkably enhanced by the introduction of the RHPC matrix. It also demonstrates that biomass-sourced carbonaceous materials like RHPC[253–255] have promising applications in LIBs due to their low cost and porous structure.[233] Tian *et al.* fabricated non-smooth carbon-coated $SnO_2$ quasi-nanocubes. Generally, in $SnO_2$/C nanocomposites, nanostructured $SnO_2$ is usually coated with smooth carbon, which is easily fabricated from organically sourced carbon *via* hydrothermal or CVD methods.[90,256] However, it is believed that $SnO_2$-coated 3D non-smooth carbon usually shows better lithium storage properties owing to the substantial free space and larger surface area of the 3D structure.[257] In this work, Tian *et al.* synthesized the hybrid nanostructures *via* multiple hydrothermal and calcination methods (Fig. 8H). As shown by the TEM images (Fig. 8I), the porous $SnO_2$ quasi-nanocubes were coated by a carbon layer with a rough surface. The introduction of 3D non-smooth carbon can reduce the transmission length of electrons and $Li^+$ and increase the electrochemical reaction sites. Based on such 3D porous structures, the $SnO_2$@C anode displayed extraordinary cycling performance and outstanding rate capability, maintaining a capacity of 1089.5 mA h $g^{-1}$ at 200 mA $g^{-1}$, even after 400 cycles, as well as 479.2 mA h $g^{-1}$ at 3000 mA $g^{-1}$.[257]

It is worth mentioning that even though the amorphous carbon layer can enhance the cycling stability and conductivity of the composites, it has a relatively low lithium storage capacity compared to $SnO_2$. Therefore, the ratio of the carbon layer and the $SnO_2$ nanomaterial determines the capacity and cycle life of the composites.

### 3.3 $SnO_2$/graphene

As an important 2D carbon material, graphene has quickly gained importance in material science in recent years. Due to its excellent mechanical properties and superior conductivity, graphene has been widely studied in LIBs.[258–260] Compared to CNTs and amorphous carbon, graphene exhibits higher specific discharge capacity, high surface area, good mechanical properties, and high chemical stability;[261–263] thus, $SnO_2$/graphene, as an anode material in LIBs, shows better electrochemical performance.[264–268]

Graphene can be used as a supporting substrate for the synthesis of hierarchical $SnO_2$ nanostructures. For example, Ding *et al.* fabricated 2D $SnO_2$ nanosheets grown on a graphene oxide (GO) support *via* a facile hydrothermal method. The $SnO_2$ nanosheets were uniformly embedded in the GO support, approximately 100 nm in length and 5–10 nm in thickness (Fig. 9A). This unique $SnO_2$/GO hybrid structure exhibited

 © 2021 The Author(s). Published by the Royal Society of Chemistry

Open Access Article. Published on 04 January 2021. Downloaded on 9/15/2024 1:15:01 AM.
This article is licensed under a Creative Commons Attribution 3.0 Unported Licence.

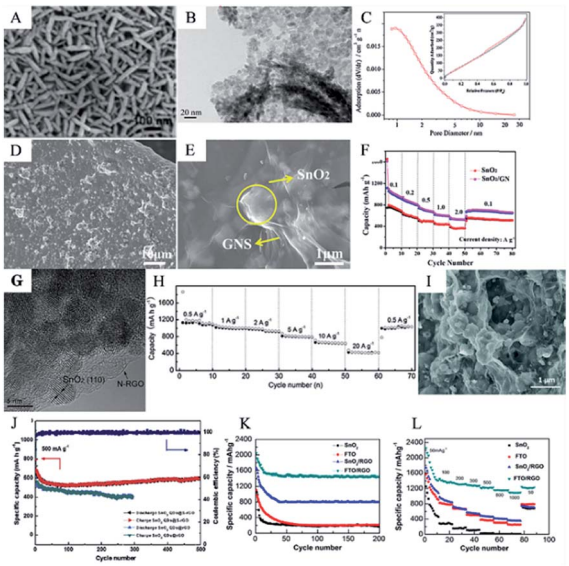


Fig. 9 (A) SEM image of $SnO_2$ nanosheets/graphene (adapted with permission from ref. 170 copyright 2011 Royal Society of Chemistry). (B) TEM image and (C) nitrogen adsorption–desorption isotherms of $SnO_2$ nanoparticles/graphene (adapted with permission from ref. 169 copyright 2017 Elsevier). (D and E) SEM images and (F) rate performance of $SnO_2$/GN on Ni foam (adapted with permission from ref. 267 copyright 2018 Elsevier). (G) HRTEM image and (H) rate performance of $SnO_2$NC@N-RGO (adapted with permission from ref. 173 copyright 2013 Wiley). (I) SEM images of $SnO_{2-x}$/N-rGO (adapted with permission from ref. 280 copyright 2018 Royal Society of Chemistry). (J) Cycling stability of $SnO_2$QDs@S-rGO (adapted with permission from ref. 277 copyright 2018 Elsevier). (K) Cycling performance and (L) rate performance of FTO/rGO (adapted with permission from ref. 109 copyright 2015 American Chemical Society).

enhanced lithium storage properties with high reversible capacities, *i.e.*, an initial discharge capacity of 1666 mA h $g^{-1}$, and good cycling performance, *i.e.*, 518 mA h $g^{-1}$ after 50 cycles at 400 mA h $g^{-1}$.[171] Additionally, due to its mechanical properties and electronic conductivity, graphene can serve as the carbon matrix to accommodate the $SnO_2$ nanoparticles. In 2017, Shi *et al.* investigated a facile microwave-assisted hydrothermal method to synthesize a composite of $SnO_2$ and graphene, which took only 30 min and did not require any chelating agents. As shown by TEM images (Fig. 9B) and the nitrogen adsorption–desorption isotherms (Fig. 9C), Shi *et al.* found that ultra-small $SnO_2$ nanoparticles were well dispersed on the surface of the graphene, with an average particle size of about 3–8 nm. It also showed superior lithium storage capability. The charge/discharge capacity of this material was 969.4/978.6 mA h $g^{-1}$ after 100 cycles at 200 mA $g^{-1}$.[269] Binder-free multilayered $SnO_2$/graphene on Ni foam was fabricated *via* a dip-coating method. $SnO_2$ nanoparticles and grapheme were alternatively coated on to the Ni foam to obtain a sandwich-like structure. As shown in SEM images in Fig. 9D and E, $SnO_2$ nanoparticles were uniformly distributed on the surface of the Ni foam and wrapped tightly in GN. Such a multilayered nanostructure showed superior electrochemical performance due to the following factors: (1) 3D porous Ni foam serves as a conductive network and binder-free current which is beneficial for electron and ion diffusion; (2) the graphene layer improves the conductivity of anode material and buffers the $SnO_2$ volume changes; and (3) the extent of volume change of the $SnO_2$ nanoparticles is lower than that of bulk $SnO_2$. Owing to such porous Ni foam frameworks and sandwich-like structures, the $SnO_2$/graphene composites exhibited good rate performance and excellent cycling stability. High capacities, *i.e.*, 708 and 609 mA h $g^{-1}$ were achieved at current densities 1 and 2 A $g^{-1}$, respectively (Fig. 9F). Furthermore, the $SnO_2$/GN electrode delivered a high capacity of 757 mA h $g^{-1}$ after 500 cycles at 1 A $g^{-1}$.[174]

Moreover, it is worth mentioning that atom-doped graphene can also be used as a carbon matrix for $SnO_2$, which effectively enhances the electrochemical performance of the composites. Heteroatoms in graphene can act as anchor sites that prevent aggregation and exfoliation of the $SnO_2$ anchored on graphene; this helps improve the cycling stability of such anode materials.[270–274] Liu *et al.* synthesized $SnO_2$ nanoparticles anchored on chlorinated graphene ($SnO_2$@rGO-Cl) as binder-free electrodes that exhibit a long cycling life, of up to 400 cycles, with a discharge capacity of 1008 mA h $g^{-1}$ *via* a facile strategy using a one-step heat treatment at low temperature.[275] Liu *et al.* found that Cl-doping can enhance the electrical conductivity of graphene and the Cl–Sn bonds can prevent the exfoliation of $SnO_2$ nanoparticles during the charge/discharge process; thus, improving the electrochemical properties of $SnO_2$-based hybrid nanomaterials. $SnO_2$/nitrogen-doped graphene (N-rGO) was also applied as an anode in LIBs. It is believed that N-doped carbonaceous materials enhance the electronic conductivity and SEI film stability.[276–278] Zhou *et al.* fabricated $SnO_2$@N-rGO *via* a hydrazine monohydrate vapor reduction approach for anchoring $SnO_2$ nanocrystals uniformly into N-rGO (Fig. 9G). Due to the bond formed between $SnO_2$ and graphene, and the void pores dispersed in N-rGO, the as-prepared hybrid materials displayed superior mechanical properties and lithium storage capacity. $SnO_2$@N-rGO anode showed a reversible charge capacity of 1346 mA h $g^{-1}$ after 500 cycles; furthermore, as the current density increased from 0.5 to 1, 2, 5, 10, and 20 A $g^{-1}$, their discharge capacity varied from 1074 to 994, 915, 782, 631, and 417 mA h $g^{-1}$, respectively (Fig. 9H).[279] Wu *et al.* synthesized the $SnO_{2-x}$/N-rGO hybrid material through electrostatic adsorption-induced self-assembly together with a thermal reduction process. This treatment induced the generation of the oxygen vacancies on the surface of $SnO_2$ hollow nanospheres; thus, building up a long-range and bi-continuous transfer channel for rapid electron and ion transport. Meanwhile, $SnO_{2-x}$ hollow spheres are well-wrapped by graphene sheets; thus, enhancing the conductivity of the anode material (Fig. 9I). Due to these structural advantages, the as-obtained $SnO_{2-x}$/N-rGO electrode exhibited excellent robust cycling stability, *i.e.*, about 912 mA h $g^{-1}$ after 500 cycles at 0.5 A $g^{-1}$ and 652 mA h $g^{-1}$ after 200 cycles at 1 A $g^{-1}$, and superior rate capability, *i.e.*, 309 mA h $g^{-1}$ at 10 A $g^{-1}$.[280] Sulfur-doped graphene (S-rGO) also proved to be a feasible anode material for LIBs.[281] Compared to the C atom, the S atom has a larger volume and lower electronegativity, which is beneficial for the diffusion of $Li^+$ and electrons. For instance, Wu *et al.* successfully loaded

Open Access Article. Published on 04 January 2021. Downloaded on 9/15/2024 1:15:01 AM.
This article is licensed under a Creative Commons Attribution 3.0 Unported Licence.

$SnO_2$ quantum dots (QDs) on sulfur-doped reduced graphene oxide (S-rGO), and it exhibited excellent lithium storage with a high specific capacity of 897 mA h $g^{-1}$ and a long cycling stability with 88% capacity retention after 500 cycles (Fig. 9J).[282] The abovementioned results demonstrate that heteroatoms can tailor the electronic structure of carbon and create topological defects in the carbon lattice.[281,283]

Apart from doped-graphene, atom-doped $SnO_2$, such as fluorine-doped tin oxide[138] and antimony-doped tin oxide[122] can also be used with pristine graphene as an anode material.[284–287] For example, Xu *et al.* has successfully fabricated composites of fluorine-doped tin oxide (FTO) and rGO from a colloidal solution containing FTO nanocrystals and rGO by a hydrothermal treatment; the FTO nanocrystals were tightly embedded in the RGO nanosheets. As an anode material, the FTO/RGO composite showed high structural stability during the lithiation and delithiation processes. The conductive FTO nanocrystals help form stable and thin SEI films. Moreover, the FTO/RGO composite retains a discharge capacity as high as 1439 mA h $g^{-1}$ after 200 cycles at 100 mA $g^{-1}$ (Fig. 9J), and 1148 mA h $g^{-1}$ at 1000 mA $g^{-1}$ (Fig. 9K).[109]

### 3.4 Complex $SnO_2$/C nanostructure

Compared to 1D or 2D carbonaceous materials, complex 3D carbonaceous matrices usually show better electrochemical properties due to their high specific surface area and porous structure, which is beneficial in suppressing volume changes.[288] In recent years, various $SnO_2$/C complex hybrid nanomaterials have been reported, such as the combination of CNTs and amorphous carbon,[288] and CNTs and graphene.[283,289,290] These complex hierarchical $SnO_2$/C nanostructures often show superior electrochemical properties, making them an important research subject.

A sandwich structure with carbon nanofiber, $SnO_2$, and nanofiber bundle for carbon-coating (C@$SnO_2$@C) has been fabricated by using collagen fiber (CF), which is a typical fibrous protein extracted from cattle skin and is used as a bio-template as well as the carbon source. FESEM image (Fig. 10A) and TEM image (Fig. 10B) show that the average diameter of the $SnO_2$ nanofiber bundle was about 5–10 μm and a layer of $SnO_2$ was sandwiched between the carbon nanofiber and the carbon coating layer. Such hierarchical architectures of the C@$SnO_2$@C nanofiber bundle guaranteed a good balance between electron transport and $Li^+$ diffusion kinetics. Thus, efficient ambipolar diffusion and reduced volume changes of $SnO_2$ were obtained to ensure structural integrity with high cycling stability.[162]

A porous 3D core–shell structured CNT@$SnO_2$ composite, with a graphene coating (CNT@$SnO_2$@G), has been synthesized *via* a two-step hydrothermal method. The first step consists of the synthesis of CNT@$SnO_2$, and then, CNT@$SnO_2$@G is formed in the subsequent step. FESEM image (Fig. 10C) and TEM image (Fig. 10D) show that CNT@$SnO_2$ (about 20–40 nm in width) particles was distributed across the graphene sheets and was encased in the graphene coating, which suppressed the formation of SEI layers on the surface of the CNT@$SnO_2$@G.

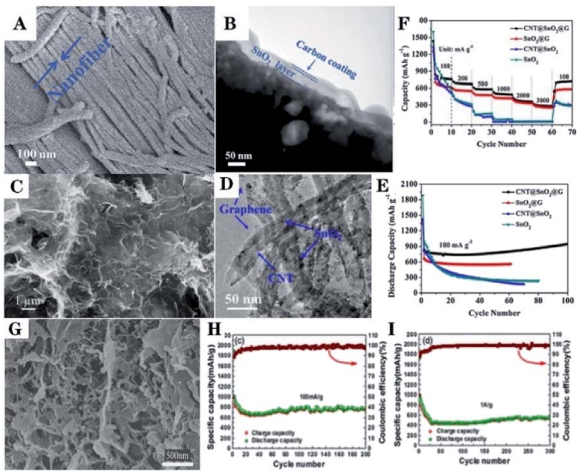


Fig. 10 (A) FESEM image, and (B) TEM image of C@$SnO_2$@C nanofiber bundle (adapted with permission from ref. 162 copyright 2016 Royal Society of Chemistry). (C) FESEM image, (D) TEM image, (E) cycling performance, and (F) rate performance of CNT@$SnO_2$@G (adapted with permission from ref. 263 copyright 2017 Elsevier). (G) SEM image, (H) cycling performance, and (I) rate performance of $SnO_2$@G-SWCNT materials (adapted with permission from ref. 289 copyright 2017 American Chemical Society).

The as-prepared CNT@$SnO_2$@G electrode exhibited outstanding lithium storage capability, including a large specific capacity, remarkable cycling stability, and excellent rate capability (Fig. 10E and F).[265]

$SnO_2$ nanoparticles anchored on an aerogel based on 3D graphene-single walled carbon nanotube ($SnO_2$@G-SWCNT), as shown in Fig. 10G, has been fabricated by a hydrothermal self-assembly process.[291] The 3D G-SWCNT matrix provides a flexible conductive matrix and a more porous network to support $SnO_2$. This is beneficial for facilitating electronic and ionic transportation and mitigating the volume changes of the $SnO_2$ during lithiation/delithiation; thus, leading to enhanced electrochemical performance of the $SnO_2$ anodes for LIBs. The discharge capacity remained 758 mA h $g^{-1}$ at 100 mA $g^{-1}$ after 200 cycles (Fig. 10H) and 537 mA h $g^{-1}$ at 1 A $g^{-1}$ after 300 cycles (Fig. 10I).[291]

## 4. $SnO_2$/TMOs/C

The composites of $SnO_2$ and transition metal oxides (TMOs) have been considered as promising anode materials for LIBs.[292–294] By the introduction of metal oxides, the reversible decomposition of $Li_2O$ can be increased because TMOs can convert extra $Li_2O$ into $Li^+$;[295–297] thus, enhancing their cycling stability, rate performance, and rate capability. However, the electrochemical performance of $SnO_2$/TMOs is unsatisfactory because of low conductivity and large volume expansion, leading to poor cycling stability.[136] In order to overcome these problems, much work has been focused on the fabrication of $SnO_2$/TMOs/C materials in recent years. Supported and coated by carbonaceous material and TMOs, the structural stability and conductivity of $SnO_2$ can be significantly improved. This

 © 2021 The Author(s). Published by the Royal Society of Chemistry

Open Access Article. Published on 04 January 2021. Downloaded on 9/15/2024 1:15:01 AM.
This article is licensed under a Creative Commons Attribution 3.0 Unported Licence.

section will cover synthesis methods, morphology, and electrochemical performance of $SnO_2$/TMOs/C.[298–302]

### 4.1 $SnO_2/Fe_2O_3/C$

$Fe_2O_3$ has been considered as another promising anode material for LIBs due to its large theoretical capacity (1007 mA h $g^{-1}$) and low cost.[303,304] However, the short carrier diffusion length inhibits lithiation/delithiation processes. It has been reported that $SnO_2/Fe_2O_3$ showed an improvement in photocatalysis, energy storage, and gas sensing.[303,305–307] Furthermore, the $SnO_2/Fe_2O_3$/C electrode showed better lithium storage capability.[308] In this composite, $SnO_2$ possesses a high intrinsic conductivity and a shortened charge diffusion distance, while $Fe_2O_3$ facilitates the reversible decomposition of $Li_2O$ and prevents Sn aggregation during charging and discharging.[309]

In 2014, Wu *et al.* proposed a facile hydrothermal method to synthesize a ternary phased $SnO_2/Fe_2O_3$/SWCNTs composite. As shown in Fig. 11A, the composites of $SnO_2$ and $Fe_2O_3$ nanoparticles were well distributed and firmly anchored on to SWCNTs, which serve as a buffer and conductive matrix. Nanosized $Fe_2O_3/SnO_2$ composites can suppress the effect of volume changes and particle agglomeration. The $SnO_2/Fe_2O_3$/SWCNTs electrode showed a high reversible capacity, superior cycle performance, and high rate capability. It delivered a capacity of 692 mA h $g^{-1}$ at 200 mA $g^{-1}$ after 50 cycles. Even at a rate as high as 2000 mA $g^{-1}$, this composite could still maintain its capacity at 656 mA h $g^{-1}$ (Fig. 11B).[310]

The growth of $SnO_2$ on $Fe_2O_3$ and subsequent carbon coating on $SnO_2/Fe_2O_3$ is another common synthesis route for $SnO_2/Fe_2O_3$/C. Du *et al.* synthesized γ-$Fe_2O_3$@$SnO_2$@C porous core–shell nanorods. They first formed FeOOH nanorods *via* a hydrothermal process, which served as a template for the subsequent $SnO_2$ deposition process in another hydrothermal system. After the deposition of $SnO_2$ on the FeOOH nanorods, the as-synthesized FeOOH@$SnO_2$ nanorods were coated with a carbon layer *via* another hydrothermal process and carbonized under $N_2$ at 500 °C for 2 h (Fig. 11C). The TEM image (Fig. 11D) shows that $SnO_2$ can successfully grow on the $Fe_2O_3$ nanostructure with well-defined interfaces. The thickness of the $SnO_2$ layer is 5–10 nm, which is composed of $SnO_2$ nanoparticles with a diameter of about 3–5 nm, and the core nanorod is highly porous. Such a porous core–shell hybrid nanorod-based electrode showed good cycling and rate performance due to the improvement of conductivity and structural stability by the introduction of carbon and $Fe_2O_3$.[115]

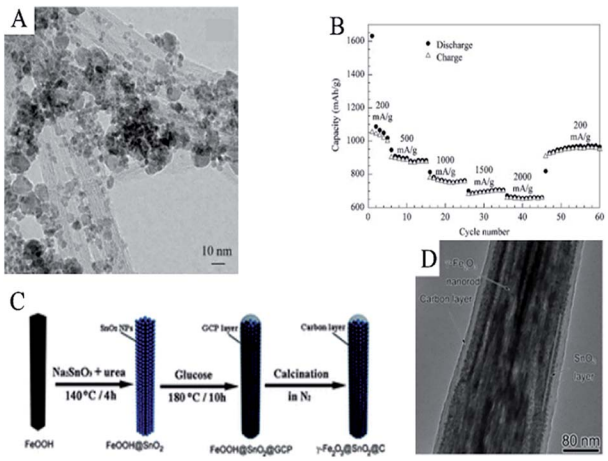


Fig. 11 (A) TEM image, and (B) rate performance of $SnO_2/Fe_2O_3$/SWCNTs (adapted with permission from ref. 308 copyright 2014 Elsevier). (C) TEM images, and (D) schematic illustration of the synthesis of γ-$Fe_2O_3$@$SnO_2$@C core–shell nanorods (adapted with permission from ref. 115 copyright 2013 Royal Society of Chemistry).

### 4.2 $SnO_2/Co_3O_4/C$

Many studies have concentrated on improving electrochemical properties of $SnO_2$ and $Co_3O_4$ by designing and synthesizing unique nanostructures. Like most transition metals, the presence of Co can improve the reversibility of the reduction reaction of $Li_2O$ and further enhance the reversible capacity.[311–315] As shown in Fig. 12A, $Co_3O_4$@$SnO_2$@C core–shell nanorods have been synthesized *via* a hydrothermal method followed by carbonization. Fig. 12B and C show that $SnO_2$ nanoparticles uniformly coated the surface of $Co_3O_4$ nanorods and that the coating was smooth and uniform, with a thickness of 5–10 nm. Such materials exhibited improved cycling performance and higher specific capability as an anode material for LIBs (860 mA h $g^{-1}$ after 50 cycles at 0.2 A $g^{-1}$). This result demonstrated that the combination of $SnO_2$ and $Co_3O_4$, into an integrated core–shell nanorod structure, exhibited a better and more elegant synergistic effect during the charge/discharge processes.

$SnO_2/Co_3O_4$@N-doped carbon (NC) usually shows better lithium storage properties compared to most $SnO_2/Co_3O_4$/C materials.[316] Wang *et al.* successfully designed and fabricated $SnO_2/Co_3O_4$/NC nanoflakes *via* a combined strategy of CVD and template synthesis.[119,317] HRTEM images (Fig. 12D) show that $SnO_2/Co_3O_4$ nanoparticles were uniformly distributed on the NC nanoflakes. By adjusting the ratio of the precursor and reaction conditions, they found that the $SnO_2/Co_3O_4$@NC ($R_{Sn/}$

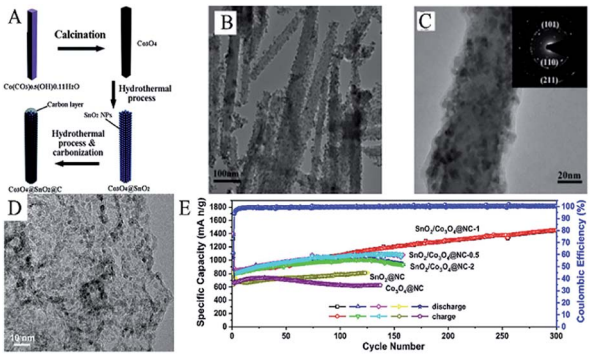


Fig. 12 (A) Schematic illustration of the fabrication of $Co_3O_4$@$SnO_2$@C core–shell nanorods. (B) TEM image, and (C) HRTEM images of $Co_3O_4$@$SnO_2$@C core–shell nanorods (adapted with permission from ref. 313 copyright 2012 Royal Society of Chemistry). (D) HRTEM image and, (E) cycling performance of $SnO_2/Co_3O_4$@NC-1 nanoflakes (adapted with permission from ref. 119 copyright 2019 Elsevier).

Open Access Article. Published on 04 January 2021. Downloaded on 9/15/2024 1:15:01 AM.
This article is licensed under a Creative Commons Attribution 3.0 Unported Licence.

$_{Co}$ = 1 : 1) nanoflakes-based electrode demonstrated excellent lithium storage capability, *i.e.*, a discharge capacity of 1450.3 mA h $g^{-1}$ after 300 cycles at 200 mA h $g^{-1}$ (Fig. 12E). The superior lithium storage of such materials may result from the synergistic effect between the combination of $SnO_2$ and $Co_3O_4$ and better conductivity caused by the N-doped carbon matrix.[119]

Therefore, in $SnO_2/Co_3O_4/C$ composites, $SnO_2$ and $Co_3O_4$ display a synergistic enhancement effect. It can provide additional active sites for lithium storage and shorten the lithium diffusion distance. Additionally, the carbon layer can greatly improve the electrode conductivity and restrain volume changes during the lithiation/delithiation processes.

### 4.3 $SnO_2/TiO_2/C$

$SnO_2$, as one of the most extensively investigated anode material, which offers a high specific capacity. However, poor cycling stability, due to large volume expansion and subsequent pulverization during $Li^+$ insertion/extraction processes, greatly restricts its application as an anode material.[130,318–320] In contrast, $TiO_2$ exhibits negligible volume change (less than 4%) and stable electrochemical properties, but its application is limited due to its low specific capacity.[321–325] Furthermore, $SnO_2$ and $TiO_2$ have complementary characteristics in LIBs, *i.e.*, $Sn^{4+}$ and $Ti^{4+}$ possess similar radii and the lattice matching of $SnO_2$ and $TiO_2$ is good.[326–328] Considering the facts mentioned above, in order to promote cycling stability of $SnO_2$, various $SnO_2/TiO_2$ based hybrid materials have been synthesized.[329–334]

Mesoporous $SnO_2$@C@$TiO_2$ nanochains have been synthesized by first fabricating $SnO_2$@C core–shell nanochains *via* a hydrothermal method and subsequent continuous mechanical stirring of the solution of $SnO_2$@C and tetrabutyl titanate ($C_{16}H_{36}O_4Ti$). It is noticeable that the $SnO_2$ core is composed of $SnO_2$ nanoparticles with a diameter of 2–6 nm and is coated by a thin carbon layer (2–6 nm) as well as a $TiO_2$ layer (about 8 nm) (Fig. 13A). In this 3D hierarchical structure, the carbon layer and the $TiO_2$ layer can effectively improve cycling stability and discharge capacity, *i.e.*, the initial discharge capacity of 807 mA h $g^{-1}$ and 369 mA h $g^{-1}$ after 100 cycles at 100 mA h $g^{-1}$.[298]

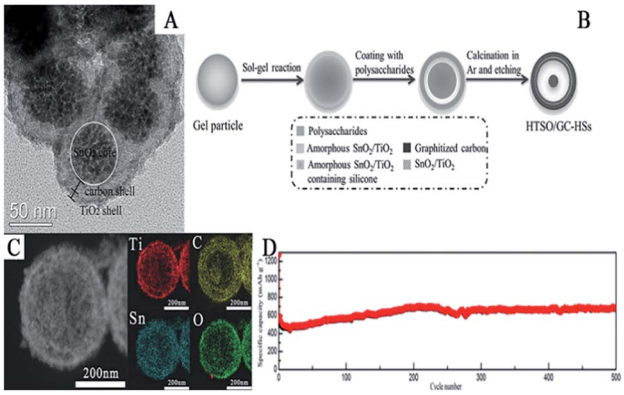


Fig. 13 (A) TEM images of $SnO_2$@C@$TiO_2$ nanochains (adapted with permission from ref. 296 copyright 2015 Elsevier). (B) Schematic illustration of the synthesis, (C) STEM image, and (D) cycling performance of HTSO/GC-HSs (adapted with permission from ref. 299 copyright 2017 Wiley).

Xie *et al.* reported the synthesis of hierarchical $TiO_2/SnO_2$ hollow spheres coated with graphitized carbon (HTSO/GC-HSs) by a multi-step approach. As shown in Fig. 13B, titanate-silicone gel particles were first reacted with $SnCl_2$ *via* a sol–gel process to obtain core–shell hybrid structures, which were further coated with a polysaccharide *via* a hydrothermal process and subsequent carbonization in Ar atmosphere. As shown in Fig. 13C, the as-prepared mesoporous HTSO/GC-HSs had a yolk–shell structure and elements Sn, Ti, O and C were found to be uniformly distributed in this hierarchical hollow nanostructure. Additionally, they also found that due to the uniform distribution of $SnO_2$, $TiO_2$, and the carbon layer, a solid solution was formed which could effectively suppress the effect of volume changes during the charge/discharge process. The specific discharge capacity remained at about 680 mA h $g^{-1}$ at 1 A $g^{-1}$ after 500 cycles, which demonstrates the excellent cycling performance of HTSO/GC-HSs at high current densities (Fig. 13D).[301]

$SnO_2/TiO_2/C$ combines the high capacity of $SnO_2$ with the long cycle life and high rate capability of $TiO_2$.[335,336] Furthermore, carbonaceous materials can inhibit agglomeration and pulverization of $SnO_2$ and enhance the conductivity of $TiO_2$.[337,338] Therefore, $SnO_2/TiO_2/C$ present an important area of research for the future.

### 4.4 $SnO_2$/TMOs/graphene

In the previous sections, we have discussed the synthesis methods, morphologies, and electrochemical performance of some representative $SnO_2$/TMOs/C anode materials. We classified them into different categories according to metal oxides because different TMOs greatly influence the physical and chemical properties of such complex materials due to different reaction mechanisms. In addition, different carbonaceous materials used in $SnO_2$/TMOs/C also influence the electrode performance in LIBs. Among these complex materials, much work has been focused on the fabrication of $SnO_2$/TMOs/graphene materials in recent years. Compared to amorphous carbon and CNTs, graphene shows higher lithium storage capacity.[339–342] Additionally, graphene, as a supportive matrix and conductive network, displays excellent mechanical properties and electronic conductivity, which is conducive to improvement in cycling stability and rate performance of $SnO_2$. Therefore, effectively combining $SnO_2$, TMOs, and graphene, to synthesize high-performance and practical anode material, has been a popular research subject in recent years.[46,275,343–345]

Wang *et al.* synthesized a $Fe_3O_4/SnO_2$/rGO (FSG) composite *via* a facile hydrothermal method. SEM images (Fig. 14A) and elemental mapping show that FSG consists of $SnO_2$ and $Fe_3O_4$ nanoparticles with diameters of about 10–100 nm, uniformly distributed on the surface of the rGO. In this composite, rGO served as a conductive and robust matrix to prevent aggregation of $Fe_3O_4$ and $SnO_2$ nanoparticles on rGO. As shown in Fig. 14B, the nanocrystallites of $Fe_3O_4$ and $SnO_2$ tend to link with each other, which is beneficial for suppressing both, *i.e.*, the

 © 2021 The Author(s). Published by the Royal Society of Chemistry

Open Access Article. Published on 04 January 2021. Downloaded on 9/15/2024 1:15:01 AM.
This article is licensed under a Creative Commons Attribution 3.0 Unported Licence.

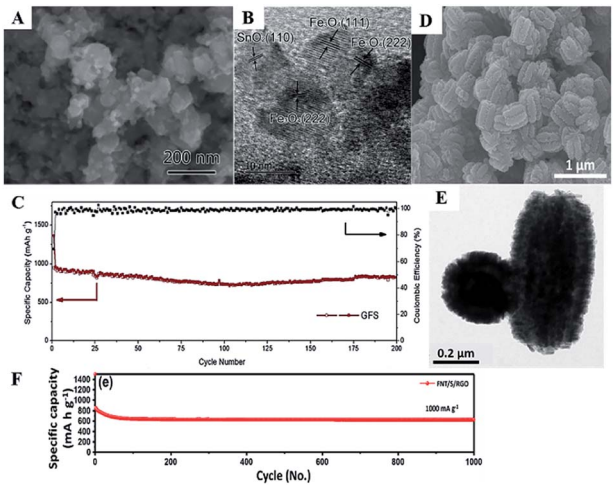


Fig. 14 (A) SEM image, (B) HRTEM image, and (C) cycling performance of FSG (adapted with permission from ref. 132 copyright 2016 Elsevier). (D) SEM image, (E) TEM image from top and side view of CNT/S, and (F) cycling performance of FNT/S/RGO (adapted with permission from ref. 136 copyright 2017 Elsevier).

formation of the SEI film and the volume changes. Such a novel nanostructure can effectively shorten the transport path of $Li^+$ and electrons and helps improve electrolyte penetration. The FSG nanocomposite exhibited a reversible capacity of 947 mA h $g^{-1}$ at a current density of 200 mA $g^{-1}$ in the first cycle and maintained a capacity of 831 mA h $g^{-1}$ after 200 cycles (Fig. 14C).[132]

Lee *et al.* have synthesized hollow nanostructured $\alpha$-$Fe_2O_3$ nanotubes/$SnO_2$/rGO (FNT/S/G) *via* a microwave-assisted hydrothermal method. As shown in Fig. 14D, $SnO_2$ nanorods grow on the surface of FNT, and FNT/$SnO_2$ are uniformly anchored on rGO sheets. The diameter and length (Fig. 14E) of FNT/S are about 230 nm and 660 nm, respectively. Lee *et al.* also compared the electrochemical performance of FNT, FNT/S, and FNT/S/G. As shown in Fig. 14F, FNT/S/G exhibited the highest discharge capacity under all tested current densities. FNT/S was the second best, demonstrating that the introduction of $SnO_2$ and rGO can effectively enhance the lithium storage capability and cycling stability of the anode material. The specific discharge capacity of FNT/S/RGO remained at 629 mA h $g^{-1}$ at 1 A $g^{-1}$ after 1000 cycles.[136,346]

Other $SnO_2$/TMOs/graphene composites like $SnO_2/TiO_2$/GN,[338] $SnO_2$/CuO/GN[347] and $SnO_2/In_2O_3$/GN[348] also exhibit improved electrochemical performance. The introduction of TMOs and graphene effectively improve the lithium storage capacity of $SnO_2$. Graphene serves as a supportive and conductive matrix that inhibits agglomeration and pulverization of $SnO_2$ and TMOs during the charge/discharge process.

## 5. Other $SnO_2$-based compounds

$Li_4Ti_5O_{12}$ (LTO) has been considered as a promising anode material for LIBs due to its excellent cycling stability during lithiation/delithiation.[349,350] However, like $TiO_2$, LTO possesses a lower theoretical capacity than other anode materials (175 mA h $g^{-1}$) and shows poor rate performance.[351,352] Therefore, in order to improve lithium storage of LTO and cycling performance of $SnO_2$, an effective strategy is to synthesize composites of $SnO_2$ and LTO nanostructures. Ding *et al.* synthesized hierarchical yolk–shell LTO–$SnO_2$ structures *via* a two-step hydrothermal method. They first synthesized $SnO_2$ microspheres at 180 °C for 12 h in a hydrothermal system and then, coated LTO on the surface of the $SnO_2$ in another hydrothermal system, followed by calcination at 600 °C for 3 h. SEM images (Fig. 15A) and TEM images (Fig. 15B) clearly show that the yolks are $SnO_2$ microspheres composed of $SnO_2$ nanoparticles, while the shells consist of LTO nanosheets. Hence, this hierarchical coating structure can effectively improve structural stability and suppress the volume changes of $SnO_2$ microspheres; thus, improving the cycling performance and showing high rate capacity.[142]

Heteroatom-doped $SnO_2$ reveals better electrochemical performance compared to pure $SnO_2$. The presence of a dopant may favor the reversible formation of $Li_2O$ and improve the conductivity of $SnO_2$; thus, enhancing the specific capacity of the anode material.[353] Various heteroatom-doped $SnO_2$ nanomaterials have been synthesized and tested as anode materials in LIBs.[354–356] For example, Mueller *et al.* have synthesized carbon-coated Fe-doped $SnO_2$ nanoparticles (Fig. 15C). The discharge capacity of such materials is about 1726 mA h $g^{-1}$ after 10 cycles at 50 mA $g^{-1}$, which is around twice the theoretical capacity of pure $SnO_2$.[353] Zn-doped $SnO_2$ hierarchical cube-like nanomaterials were fabricated *via* hydrothermal method. As shown in Fig. 15D and E, the cube is about 2 μm in length and composed of assembled nanorods which are 20–40 nm in diameter. The discharge capacity of Zn-doped $SnO_2$

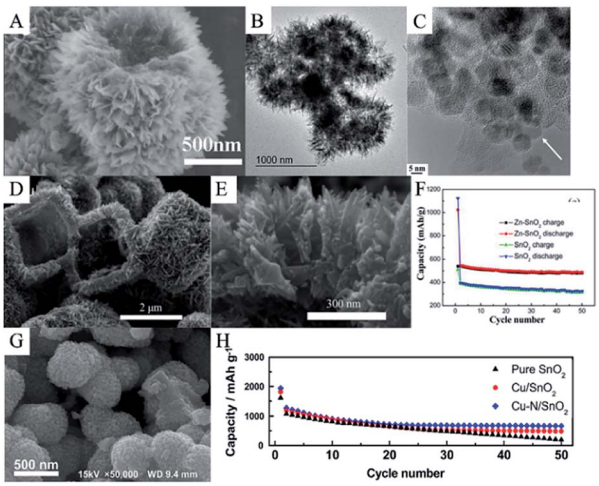


Fig. 15 5(A) SEM image, and (B) TEM image of LTO–$SnO_2$ composites (adapted with permission from ref. 142 copyright 2018 Elsevier). (C) HRTEM image of carbon-coated Fe-doped $SnO_2$ nanoparticles (adapted with permission from ref. 351 copyright 2015 Elsevier). (D and E) SEM images, and (F) cycling performance of Zn-doped $SnO_2$ nanomaterials (adapted with permission from ref. 355 copyright 2014 Elsevier). (G) SEM image, and (H) cycling performance of Cu/N-doped $SnO_2$ (adapted with permission from ref. 139 copyright 2014 Elsevier).

Open Access Article. Published on 04 January 2021. Downloaded on 9/15/2024 1:15:01 AM.
This article is licensed under a Creative Commons Attribution 3.0 Unported Licence.

Table 1 Electrochemical property comparison table of some typical $SnO_2$-based anode materials for LIBs

| Materials | Morphology | Preparation approach | Voltage window (V) | Current density (A $g^{-1}$) | Cycle number | Specific capacity (mA h $g^{-1}$) | Reference |
|---|---|---|---|---|---|---|---|
| $SnO_2$ nanorods | Diameter of 60 nm and length of 670 nm | Hydrothermal | 0.005–2.5 | 0.078 | 100 | 580 | 154 |
| $SnO_2$ nanotube arrays | Diameter of 100–300 nm and thickness of 10–20 nm | Solvothermal and annealing | 0.005–2 | 0.078 | 20 | 750–800 | 64 |
| $SnO_2$ nanowires | Diameter of 6 nm and length of >3 μm | Solvothermal and annealing | 0–1.2 | 0.156 | 50 | 773 | 71 |
| $SnO_2$ nanosheet arrays | Thickness of 20 nm and length of 500 nm | Hydrothermal | 0.01–1.2 | 0.391 | 50 | 674.9 | 79 |
| Hollow $SnO_2$ nanospheres | Size of 100–250 nm | Solvothermal and hydrothermal | 0.01–2 | 0.391 | 40 | 1140 | 86 |
| Urchin-like $SnO_2$ nanospheres | Diameter of 300 nm | Solvothermal | 0.01–3 | 0.1 | 50 | 719 | 210 |
| $SnO_2$ nanocrystals/MWCNT composites | Crystal size of 5 nm | Solvothermal and heat treatment | 0.01–3 | 0.1 | 100 | 402 | 223 |
| CNT@void@$SnO_2$@C | Tube in tube diameter of 100–150 nm | Spray drying | 0.01–3 | 0.2 | 350 | 702.5 | 226 |
| $SnO_2$/C composite hollow spheres | Size of 150–400 nm | Hydrothermal and carbonation | 0–2.5 | 0.16 | 50 | 473 | 99 |
| $SnO_2$ nanoparticles/carbon composite | Nanoparticles of 5–10 nm | Polyol method | 0.005–1.5 | 0.2 | 100 | 370 | 251 |
| $SnO_2$ nanosheets/GO | Length of 100 nm and thickness of 5–10 nm | Hydrothermal | 0.01–1.2 | 0.4 | 50 | 518 | 171 |
| $SnO_2$ nanoparticles/graphene | Particle size of 3–8 nm | Microwave-assisted hydrothermal | 0.01–3 | 0.2 | 100 | 978.6 | 269 |
| $SnO_2$@rGO-Cl | Nanoparticle size of 5 nm | Heat treatment | 0.01–3 | 0.2 | 400 | 1008 | 275 |
| CNT@$SnO_2$@G | Width of 20–40 nm | Hydrothermal | 0.01–3 | 0.1 | 100 | 947 | 265 |
| $SnO_2$@G-SWCNT | Diameter of 3–5 nm and particle size of 6–8 nm | Hydrothermal | 0.01–3 | 1 | 300 | 537 | 291 |
| $SnO_2$–$Fe_2O_3$/SWCNTs nanocomposite | Particle size of 10–50 nm | Hydrothermal | 0.01–3 | 0.2 | 50 | 692 | 310 |
| $Co_3O_4$@$SnO_2$@C core–shell nanorods | Thickness of 5–10 nm | Hydrothermal | 0.01–2.5 | 0.2 | 50 | 860 | 313 |
| $SnO_2$@C@$TiO_2$ nanochains | $SnO_2$ for 2–6 nm; thickness of 2–6 nm and 8 nm for carbon and $TiO_2$ | Hydrothermal and subsequent mechanical stirring | 0.01–3 | 0.1 | 100 | 369 | 298 |
| $Fe_2O_3$ nanotubes/$SnO_2$/rGO | Diameter of 230 nm and length of 660 nm | Microwave-assisted hydrothermal | 0.01–3 | 1 | 1000 | 629 | 136 |
| Yolk–shell LTO–$SnO_2$ | Diameter of 1.0–1.5 μm | Hydrothermal and calcination | 0.01–3 | 0.175 | 200 | 253.2 | 142 |
| Fe-doped $SnO_2$ nanoparticles | Diameter of 15 nm | Hydrothermal and calcination | 0.01–2 | 0.05 | 10 | 1726 | 351 |

composites is 488.3 mA h $g^{-1}$ after 50 cycles at 10 mA $g^{-1}$ (Fig. 15F).[357] Wan *et al.* fabricated Cu/N-doped $SnO_2$ nanocomposites, as shown in Fig. 15G. They found that with the introduction of Cu/N, the average diameter of $SnO_2$ became smaller, and the surface became rough, which is beneficial for ion diffusion and suppressing volume expansion. Cu/N-doped $SnO_2$ electrode materials are known to deliver a discharge capacity of 1939 mA h $g^{-1}$ in the first cycle and remain at 664 mA h $g^{-1}$ after 50 cycles at 0.1C.[139]

## 6. Conclusions

In this review, we summarized various $SnO_2$-based nanomaterials as anode materials for lithium-ion batteries (Table 1). By optimizing the structure and composition of the materials, *i.e.*, by synthesizing nanostructured $SnO_2$ and making composites with carbonaceous materials or transition metal oxides (TMOs), the surface area and reaction sites of the anode materials can be effectively increased, improving the electrochemical properties of $SnO_2$-based anode materials. The introduction of carbonaceous materials or TMOs can effectively buffer the internal stresses caused by large volume changes, reduce the irreversible capacity loss, and improve the cycle performance. These aspects lay the foundation for the development and commercialization of high-performance LIBs in the future. Since lithium storage in $SnO_2$ is accompanied by repeatedly inserting and removing lithium ions, volume changes and irreversible capacity loss of $SnO_2$ electrode cannot

 © 2021 The Author(s). Published by the Royal Society of Chemistry

Open Access Article. Published on 04 January 2021. Downloaded on 9/15/2024 1:15:01 AM.
This article is licensed under a Creative Commons Attribution 3.0 Unported Licence.

be completely avoided. Significant research on nanosized $SnO_2$-based anode materials has been carried out, and while these materials display superior lithium storage capacity and cycling stability, critical issues like volume expansion and pulverization of $SnO_2$ remain to be solved. Further extensive research is needed before new, non-carbonaceous anode materials, such as $SnO_2$-based nanomaterials, can be commercialized.

## Conflicts of interest

There are no conflicts to declare.

## Acknowledgements

This research was supported by the National Key Research and Development Project (Grant No. 2020YFB1506001), Major Project of Education Department in Sichuan (Grant No. 18ZB0229), Sichuan Province Science and Technology Support Program (Grant No. 18ZDYF2973).

## References

1 J. M. Tarascon and M. Armand, *Nature*, 2001, **414**, 359–367.
2 N. Nitta, F. Wu, J. T. Lee and G. Yushin, *Mater. Today*, 2015, **18**, 252–264.
3 M. V. Reddy, G. V. S. Rao and B. V. R. Chowdari, *Chem. Rev.*, 2013, **113**, 5364–5457.
4 V. Etacheri, R. Marom, R. Elazari, G. Salitra and D. Aurbach, *Energy Environ. Sci.*, 2011, **4**, 3243–3262.
5 C. Liu, F. Li, L. P. Ma and H. M. Cheng, *Adv. Mater.*, 2010, **22**, E28–E62.
6 M.-S. Kim, B. Fang, J. H. Kim, D. Yang, Y. K. Kim, T.-S. Bae and J.-S. Yu, *J. Mater. Chem.*, 2011, **21**, 19362–19367.
7 W. Li, L. Zhao, Y. Tian, Y. Gong, X. Huang, Z. Cui and R. Zeng, *Electrochim. Acta*, 2014, **147**, 603–609.
8 J. Cabana, L. Monconduit, D. Larcher and M. Rosa Palacin, *Adv. Mater.*, 2010, **22**, E170–E192.
9 A. Magasinski, P. Dixon, B. Hertzberg, A. Kvit, J. Ayala and G. Yushin, *Nat. Mater.*, 2010, **9**, 353–358.
10 B. Scrosati, J. Hassoun and Y.-K. Sun, *Energy Environ. Sci.*, 2011, **4**, 3287–3295.
11 B. Fang, M.-S. Kim, J. H. Kim, S. Lim and J.-S. Yu, *J. Mater. Chem.*, 2010, **20**, 10253–10259.
12 J. B. Goodenough and Y. Kim, *Chem. Mater.*, 2010, **22**, 587–603.
13 J. Jiang, Y. Li, J. Liu, X. Huang, C. Yuan and X. W. Lou, *Adv. Mater.*, 2012, **24**, 5166–5180.
14 K. Chang and W. Chen, *ACS Nano*, 2011, **5**, 4720–4728.
15 Y. Sun, Q. Wu and G. Shi, *Energy Environ. Sci.*, 2011, **4**, 1113–1132.
16 Z.-S. Wu, G. Zhou, L.-C. Yin, W. Ren, F. Li and H.-M. Cheng, *Nano Energy*, 2012, **1**, 107–131.
17 C. Yuan, H. B. Wu, Y. Xie and X. W. Lou, *Angew. Chem., Int. Ed.*, 2014, **53**, 1488–1504.
18 N. Liu, Z. Lu, J. Zhao, M. T. McDowell, H.-W. Lee, W. Zhao and Y. Cui, *Nat. Nanotechnol.*, 2014, **9**, 187–192.
19 J. B. Goodenough and K.-S. Park, *J. Am. Chem. Soc.*, 2013, **135**, 1167–1176.
20 P. G. Bruce, S. A. Freunberger, L. J. Hardwick and J.-M. Tarascon, *Nat. Mater.*, 2012, **11**, 19–29.
21 Y. Deng, C. Fang and G. Chen, *J. Power Sources*, 2016, **304**, 81–101.
22 L. Lu, X. Han, J. Li, J. Hua and M. Ouyang, *J. Power Sources*, 2013, **226**, 272–288.
23 J. W. Choi and D. Aurbach, *Nat. Rev. Mater.*, 2016, **1**, 16013.
24 W.-B. Hua, X.-D. Guo, Z. Zheng, Y.-J. Wang, B.-H. Zhong, B. Fang, J.-Z. Wang, S.-L. Chou and H. Liu, *J. Power Sources*, 2015, **275**, 200–206.
25 Y. Xing, S. Wang, B. Fang, Y. Feng and S. Zhang, *Microporous Mesoporous Mater.*, 2018, **261**, 237–243.
26 W. Hua, Y. Wang, Y. Zhong, G. Wang, B. Zhong, B. Fang, X. Guo, S. Liao and H. Wang, *Chin. J. Chem.*, 2015, **33**, 261–267.
27 F. Cheng, Y. Chen, A. Sun, X. Zhou, J. Yang and J. Tang, *Ceram. Int.*, 2019, **45**, 13556–13560.
28 J. Jia, X. Hu and Z. Wen, *Nano Res.*, 2018, **11**, 1135–1145.
29 T. Wang, H. Li, S. Shi, T. Liu, G. Yang, Y. Chao and F. Yin, *Small*, 2017, **13**, 1604182.
30 G. Xu, L. Zhang, C. Guo, L. Gu, X. Wang, P. Han, K. Zhang, C. Zhang and G. Cui, *Electrochim. Acta*, 2012, **85**, 345–351.
31 H. Xia, M. Lai and L. Lu, *J. Mater. Chem.*, 2010, **20**, 6896–6902.
32 A. L. M. Reddy, M. M. Shaijumon, S. R. Gowda and P. M. Ajayan, *Nano Lett.*, 2009, **9**, 1002–1006.
33 J. Zhu and J. He, *ACS Appl. Mater. Interfaces*, 2012, **4**, 1770–1776.
34 H. Xu, X. Hu, H. Yang, Y. Sun, C. Hu and Y. Huang, *Adv. Energy Mater.*, 2015, **5**, 1401882.
35 B. Sun, Z. Chen, H.-S. Kim, H. Ahn and G. Wang, *J. Power Sources*, 2011, **196**, 3346–3349.
36 D. Kong, J. Luo, Y. Wang, W. Ren, T. Yu, Y. Luo, Y. Yang and C. Cheng, *Adv. Funct. Mater.*, 2014, **24**, 3815–3826.
37 S. Zhu, J. Li, X. Deng, C. He, E. Liu, F. He, C. Shi and N. Zhao, *Adv. Funct. Mater.*, 2017, **27**, 1605017.
38 H. Wang, L.-F. Cui, Y. Yang, H. S. Casalongue, J. T. Robinson, Y. Liang, Y. Cui and H. Dai, *J. Am. Chem. Soc.*, 2010, **132**, 13978–13980.
39 J. Gao, M. A. Lowe and H. D. Abruna, *Chem. Mater.*, 2011, **23**, 3223–3227.
40 Z. Cai, L. Xu, M. Yan, C. Han, L. He, K. M. Hercule, C. Niu, Z. Yuan, W. Xu, L. Qu, K. Zhao and L. Mai, *Nano Lett.*, 2015, **15**, 738–744.
41 X. Zhu, Y. Zhu, S. Murali, M. D. Stollers and R. S. Ruoff, *ACS Nano*, 2011, **5**, 3333–3338.
42 L. Zhang, H. B. Wu, S. Madhavi, H. H. Hng and X. W. Lou, *J. Am. Chem. Soc.*, 2012, **134**, 17388–17391.
43 X. Xu, R. Cao, S. Jeong and J. Cho, *Nano Lett.*, 2012, **12**, 4988–4991.
44 Z. Wang, D. Luan, S. Madhavi, Y. Hu and X. W. Lou, *Energy Environ. Sci.*, 2012, **5**, 5252–5256.
45 M. V. Reddy, T. Yu, C.-H. Sow, Z. X. Shen, C. T. Lim, G. V. S. Rao and B. V. R. Chowdari, *Adv. Funct. Mater.*, 2007, **17**, 2792–2799.

Open Access Article. Published on 04 January 2021. Downloaded on 9/15/2024 1:15:01 AM.
This article is licensed under a Creative Commons Attribution 3.0 Unported Licence.

46 G. Zhou, D.-W. Wang, F. Li, L. Zhang, N. Li, Z.-S. Wu, L. Wen, G. Q. Lu and H.-M. Cheng, *Chem. Mater.*, 2010, **22**, 5306–5313.
47 W.-M. Zhang, X.-L. Wu, J.-S. Hu, Y.-G. Guo and L.-J. Wan, *Adv. Funct. Mater.*, 2008, **18**, 3941–3946.
48 W. Wei, S. Yang, H. Zhou, I. Lieberwirth, X. Feng and K. Muellen, *Adv. Mater.*, 2013, **25**, 2909–2914.
49 J. Luo, J. Liu, Z. Zeng, C. F. Ng, L. Ma, H. Zhang, J. Lin, Z. Shen and H. J. Fan, *Nano Lett.*, 2013, **13**, 6136–6143.
50 C. He, S. Wu, N. Zhao, C. Shi, E. Liu and J. Li, *ACS Nano*, 2013, **7**, 4459–4469.
51 X. Wang, X.-L. Wu, Y.-G. Guo, Y. Zhong, X. Cao, Y. Ma and J. Yao, *Adv. Funct. Mater.*, 2010, **20**, 1680–1686.
52 X. W. Lou, D. Deng, J. Y. Lee, J. Feng and L. A. Archer, *Adv. Mater.*, 2008, **20**, 258–262.
53 Y. Li, B. Tan and Y. Wu, *Nano Lett.*, 2008, **8**, 265–270.
54 W. Y. Li, L. N. Xu and J. Chen, *Adv. Funct. Mater.*, 2005, **15**, 851–857.
55 W. M. Zhang, J. S. Hu, Y. G. Guo, S. F. Zheng, L. S. Zhong, W. G. Song and L. J. Wan, *Adv. Mater.*, 2008, **20**, 1160–1165.
56 X. W. Lou, Y. Wang, C. L. Yuan, J. Y. Lee and L. A. Archer, *Adv. Mater.*, 2006, **18**, 2325–2329.
57 X. W. Lou, C. M. Li and L. A. Archer, *Adv. Mater.*, 2009, **21**, 2536–2539.
58 C. Guo, M. Cao and C. Hu, *Inorg. Chem. Commun.*, 2004, **7**, 929–931.
59 B. Liu, J.-G. Zhang and W. Xu, *Joule*, 2018, **2**, 833–845.
60 I. A. Courtney, *J. Electrochem. Soc.*, 1997, **144**, 2045.
61 X. Zhou, L.-J. Wan and Y.-G. Guo, *Adv. Mater.*, 2013, **25**, 2152–2157.
62 H. Kim, G. O. Park, Y. Kim, S. Muhammad, J. Yoo, M. Balasubramanian, Y.-H. Cho, M.-G. Kim, B. Lee, K. Kang, H. Kim, J. M. Kim and W.-S. Yoon, *Chem. Mater.*, 2014, **26**, 6361–6370.
63 M.-S. Park, G.-X. Wang, Y.-M. Kang, D. Wexler, S.-X. Dou and H.-K. Liu, *Angew. Chem., Int. Ed.*, 2007, **46**, 750–753.
64 J. Wang, N. Du, H. Zhang, J. Yu and D. Yang, *J. Phys. Chem. C*, 2011, **115**, 11302–11305.
65 Y. Wang, M. Wu, Z. Jiao and J. Y. Lee, *Nanotechnology*, 2009, **20**, 345704.
66 M. Lai, J. A. Gonzalez Martinez, M. Grätzel and D. J. Riley, *J. Mater. Chem.*, 2006, **16**, 2843–2845.
67 N. Du, H. Zhang, B. Chen, X. Ma and D. Yang, *Chem. Commun.*, 2008, 3028–3030.
68 Y. Wang, J. Y. Lee and H. C. Zeng, *Chem. Mater.*, 2005, **17**, 3899–3903.
69 S. J. Ding, Z. Y. Wang, S. Madhavi and X. W. Lou, *J. Mater. Chem.*, 2011, **21**, 13860–13864.
70 Y. T. Han, X. Wu, Y. L. Ma, L. H. Gong, F. Y. Qu and H. J. Fan, *CrystEngComm*, 2011, **13**, 3506–3510.
71 H. Kim and J. Cho, *J. Mater. Chem.*, 2008, **18**, 771–775.
72 Y. D. Ko, J. G. Kang, J. G. Park, S. Lee and D. W. Kim, *Nanotechnology*, 2009, **20**, 455701.
73 W. Ren, C. Wang, L. Lu, D. Li, C. Cheng and J. Liu, *J. Mater. Chem. A*, 2013, **1**, 13433–13438.
74 Q. Wan, E. N. Dattoli and W. Lu, *Appl. Phys. Lett.*, 2007, **90**, 222107.
75 Q. Tian, L. Li, J. Chen, L. Yang and S.-i. Hirano, *J. Power Sources*, 2018, **376**, 1–10.
76 X. Zhu, H. Shi, J. Yin, H. Zhu, Y. Zhou, Y. Tang, P. Wu and T. Lu, *RSC Adv.*, 2014, **4**, 34417–34420.
77 L. Zhang, H. B. Wu and X. Wen Lou, *Mater. Horiz.*, 2014, **1**, 133–138.
78 S. Zhang, B. Yin, Y. Jiao, Y. Liu, F. Qu and X. Wu, *Appl. Surf. Sci.*, 2014, **305**, 626–629.
79 X. Zhao, B. Liu, C. Hu and M. Cao, *Chemistry*, 2014, **20**, 467–473.
80 Y. Zhu, H. Guo, H. Zhai and C. Cao, *ACS Appl. Mater. Interfaces*, 2015, **7**, 2745–2753.
81 W. Wei, P. Du, D. Liu, H. Wang and P. Liu, *J. Colloid Interface Sci.*, 2017, **503**, 205–213.
82 B. Kumar, D. H. Lee, S. H. Kim, B. Yang, S. Maeng and S. W. Kim, *J. Phys. Chem. C*, 2010, **114**, 11050–11055.
83 G. D. Park, J.-K. Lee and Y. C. Kang, *Adv. Funct. Mater.*, 2017, **27**, 222107.
84 J. H. Kim, K. M. Jeon, J.-S. Park and Y. C. Kang, *J. Power Sources*, 2017, **359**, 363–370.
85 J.-S. Park, Y. J. Oh, J. H. Kim and Y. C. Kang, *Mater. Charact.*, 2020, **161**, 222107.
86 X. W. Lou, Y. Wang, C. Yuan, J. Y. Lee and L. A. Archer, *Adv. Mater.*, 2006, **18**, 2325–2329.
87 S. Ding and X. Wen Lou, *Nanoscale*, 2011, **3**, 3586–3588.
88 H. Wang, F. Fu, F. Zhang, H.-E. Wang, S. V. Kershaw, J. Xu, S.-G. Sun and A. L. Rogach, *J. Mater. Chem.*, 2012, **22**, 2140–2148.
89 Y. Wang, T. Su, H. Chen, W. Liu, Y. Dong and S. Hu, *Mater. Lett.*, 2014, **137**, 241–244.
90 J. Qin, N. Zhao, C. Shi, E. Liu, F. He, L. Ma, Q. Li, J. Li and C. He, *J. Mater. Chem. A*, 2017, **5**, 10946–10956.
91 W.-S. Kim, Y. Hwa, J.-H. Jeun, H.-J. Sohn and S.-H. Hong, *J. Power Sources*, 2013, **225**, 108–112.
92 J. Zhang, H. Ren, J. Wang, J. Qi, R. Yu, D. Wang and Y. Liu, *J. Mater. Chem. A*, 2016, **4**, 17673–17677.
93 L.-Y. Jiang, X.-L. Wu, Y.-G. Guo and L.-J. Wan, *J. Phys. Chem. C*, 2009, **113**, 14213–14219.
94 H.-X. Zhang, C. Feng, Y.-C. Zhai, K.-L. Jiang, Q.-Q. Li and S.-S. Fan, *Adv. Mater.*, 2009, **21**, 2299–2304.
95 W. Dong, J. Xu, C. Wang, Y. Lu, X. Liu, X. Wang, X. Yuan, Z. Wang, T. Lin, M. Sui, I. W. Chen and F. Huang, *Adv. Mater.*, 2017, **29**, 1700136.
96 C. Zhang, X. Peng, Z. Guo, C. Cai, Z. Chen, D. Wexler, S. Li and H. Liu, *Carbon*, 2012, **50**, 1897–1903.
97 W. Long, B. Fang, A. Ignaszak, Z. Wu, Y.-J. Wang and D. Wilkinson, *Chem. Soc. Rev.*, 2017, **46**, 7176–7190.
98 L. Noerochim, J.-Z. Wang, S.-L. Chou, H.-J. Li and H.-K. Liu, *Electrochim. Acta*, 2010, **56**, 314–320.
99 X. W. Lou, D. Deng, J. Y. Lee and L. A. Archer, *Chem. Mater.*, 2008, **20**, 6562–6566.
100 Z. Wen, Q. Wang, Q. Zhang and J. Li, *Adv. Funct. Mater.*, 2007, **17**, 2772–2778.
101 D. Guan, J. Li, X. Gao and C. Yuan, *RSC Adv.*, 2015, **5**, 58514–58521.

 © 2021 The Author(s). Published by the Royal Society of Chemistry

Open Access Article. Published on 04 January 2021. Downloaded on 9/15/2024 1:15:01 AM.
This article is licensed under a Creative Commons Attribution 3.0 Unported Licence.

102 X. Zhou, W. Liu, X. Yu, Y. Liu, Y. Fang, S. Klankowski, Y. Yang, J. E. Brown and J. Li, *ACS Appl. Mater. Interfaces*, 2014, **6**, 7434–7443.
103 J. S. Chen, Y. L. Cheah, Y. T. Chen, N. Jayaprakash, S. Madhavi, Y. H. Yang and X. W. Lou, *J. Phys. Chem. C*, 2009, **113**, 20504–20508.
104 X. Zhao, Z. Zhang, F. Yang, Y. Fu, Y. Lai and J. Li, *RSC Adv.*, 2015, **5**, 31465–31471.
105 J. Cheng, H. Xin, H. Zheng and B. Wang, *J. Power Sources*, 2013, **232**, 152–158.
106 H. Song, N. Li, H. Cui and C. Wang, *J. Mater. Chem. A*, 2013, **1**, 7558–7562.
107 H. Liu, J. Huang, X. Li, J. Liu, Y. Zhang and K. Du, *Appl. Surf. Sci.*, 2012, **258**, 4917–4921.
108 L. Fan, X. Li, B. Yan, X. Li, D. Xiong, D. Li, H. Xu, X. Zhang and X. Sun, *Appl. Energy*, 2016, **175**, 529–535.
109 H. Xu, L. Shi, Z. Wang, J. Liu, J. Zhu, Y. Zhao, M. Zhang and S. Yuan, *ACS Appl. Mater. Interfaces*, 2015, **7**, 27486–27493.
110 J. Liu, J. Huang, L. Hao, H. Liu and X. Li, *Ceram. Int.*, 2013, **39**, 8623–8627.
111 H. Xu, J. Chen, D. Wang, Z. Sun, P. Zhang, Y. Zhang and X. Guo, *Carbon*, 2017, **124**, 565–575.
112 B. Fang, J. H. Kim, M.-S. Kim and J.-S. Yu, *Acc. Chem. Res.*, 2013, **46**, 1397–1406.
113 Y. Xing, Y. Wang, C. Zhou, S. Zhang and B. Fang, *ACS Appl. Mater. Interfaces*, 2014, **6**, 2561–2567.
114 J. Lu, D. Qi, C. Deng, X. Zhang and P. Yang, *Nanoscale*, 2010, **2**, 1892–1900.
115 N. Du, Y. Chen, C. Zhai, H. Zhang and D. Yang, *Nanoscale*, 2013, **5**, 4744–4750.
116 F. Li, G. Luo, J. Yu, W. Huang, D. Xu, W. Chen, X. Huang, S. Yang, Y. Fang and X. Yu, *J. Alloys Compd.*, 2019, **773**, 778–787.
117 X. Wu, W. Wu, Y. Zhou, X. Huang, W. Chen and Q. Wang, *Powder Technol.*, 2015, **280**, 119–123.
118 M. Huang, X. L. Zhao, F. Li, W. Li, B. Zhang and Y. X. Zhang, *J. Mater. Chem. A*, 2015, **3**, 12852–12857.
119 J. Wang, H. Wang, T. Yao, T. Liu, Y. Tian, C. Li, F. Li, L. Meng and Y. Cheng, *J. Colloid Interface Sci.*, 2020, **560**, 546–554.
120 D. Deng, M. G. Kim, J. Y. Lee and J. Cho, *Energy Environ. Sci.*, 2009, **2**, 818–837.
121 Z. Yang, G. Du, Z. Guo, X. Yu, Z. Chen, T. Guo and R. Zeng, *Nanoscale*, 2011, **3**, 4440–4447.
122 A. Ansari and D. Nematollahi, *Appl. Catal., B*, 2020, **261**, 118226.
123 B. Zhao, F. Mattelaer, J. Kint, A. Werbrouck, L. Henderick, M. Minjauw, J. Dendooven and C. Detavernier, *Electrochim. Acta*, 2019, **320**, 134604.
124 L. L. Si, Z. Q. Yuan, J. W. Liang, L. Hu, Y. C. Zhu and Y. T. Qian, *J. Mater. Chem. A*, 2014, **2**, 9784–9791.
125 L.-J. Xue, Y.-F. Xu, L. Huang, F.-S. Ke, Y. He, Y.-X. Wang, G.-Z. Wei, J.-T. Li and S.-G. Sun, *Electrochim. Acta*, 2011, **56**, 5979–5987.
126 H. El-Shinawi, A. S. Schulze, M. Neumeier, T. Leichtweiß and J. Janek, *J. Phys. Chem. C*, 2014, **118**, 8818–8823.
127 Q. Tian, Y. Chen, F. Zhang, W. Zhang, Z. Sui and L. Yang, *Appl. Surf. Sci.*, 2020, **511**, 145625.
128 M. Jayalakshmi, M. M. Rao, N. Venugopal and K.-B. Kim, *J. Power Sources*, 2007, **166**, 578–583.
129 Q. Guo, Z. Sun, M. Gao, Z. Tan, B. Zhang and D. S. Su, *J. Energy Chem.*, 2013, **22**, 347–355.
130 D. Wei, S. Zhong, H. Zhang, X. Zhang, C. Zhu, J. Duan, L. Li, Z. Chen, P. Liu, G. Zhang and H. Duan, *Electrochim. Acta*, 2018, **290**, 312–321.
131 G. Wen, H. Liu, T. Liang, Y. Ouyang, L. Tan, R. Hu, J. Liu, Y. Zhang and M. Zhu, *Electrochim. Acta*, 2020, **334**, 135640.
132 Y. Wang, H. Zhang, R. Hu, J. Liu, T. van Ree, H. Wang, L. Yang and M. Zhu, *J. Alloys Compd.*, 2017, **693**, 1174–1179.
133 W. Guo, Y. Wang, F. Zhang, S. Rao, P. Mao and D. Wang, *Energy Fuels*, 2020, **34**, 2462–2470.
134 L. Si, Z. Yuan, J. Liang, L. Hu, Y. Zhu and Y. Qian, *J. Mater. Chem. A*, 2014, **2**, 9784–9791.
135 D. Cao, H. Wang, B. Li, C. Li, S. Xie, A. L. Rogach and C. Niu, *Electrochim. Acta*, 2016, **216**, 79–87.
136 K. Lee, S. Shin, T. Degen, W. Lee and Y. S. Yoon, *Nano Energy*, 2017, **32**, 397–407.
137 X. Liu, F. Liu, Q. Sun, A. M. Ng, A. B. Djurisic, M. Xie, C. Liao, K. Shih and Z. Deng, *ACS Appl. Mater. Interfaces*, 2014, **6**, 13478–13486.
138 H.-S. Oh, H. N. Nong and P. Strasser, *Adv. Funct. Mater.*, 2015, **25**, 1074–1081.
139 N. Wan, P. Yu, S. Sun, Q. Wu, T. Li and Y. Bai, *Mater. Lett.*, 2014, **133**, 168–170.
140 X. Liu, G. Zhou, S. W. Or and Y. Sun, *RSC Adv.*, 2014, **4**, 51389–51394.
141 A. Vignesh, A. S. Siddarth, O. S. Gokul and B. R. Babu, *Int. J. Environ. Sci. Technol.*, 2014, **11**, 1669–1678.
142 M. Ding, H. Liu, J. Zhu, X. Zhao, L. Pang, Y. Qin and L. Deng, *Appl. Surf. Sci.*, 2018, **448**, 389–399.
143 V. Vo, X. D. Nguyen Thi, Y.-S. Jin, G. Ly Thi, T. T. Nguyen, T. Q. Duong and S.-J. Kim, *Chem. Phys. Lett.*, 2017, **674**, 42–47.
144 J. Liu, Y. Li, X. Huang, R. Ding, Y. Hu, J. Jiang and L. Liao, *J. Mater. Chem.*, 2009, **19**, 1859–1864.
145 Y. J. Chen, X. Y. Xue, Y. G. Wang and T. H. Wang, *Appl. Phys. Lett.*, 2005, **87**, 233503.
146 W. Xu, K. Zhao, C. Niu, L. Zhang, Z. Cai, C. Han, L. He, T. Shen, M. Yan, L. Qu and L. Mai, *Nano Energy*, 2014, **8**, 196–204.
147 J. Ye, H. Zhang, R. Yang, X. Li and L. Qi, *Small*, 2010, **6**, 296–306.
148 D. F. Zhang, L. D. Sun, J. L. Yin and C. H. Yan, *Adv. Mater.*, 2003, **15**, 1022–1025.
149 C. Yang, G. Zhang, L. Zhang and L. Ma, in *Advances In Composites, Pts 1 and 2*, ed. J. L. Bu, Z. Y. Jiang and S. Jiao, 2011, vol. 150–151, pp. 1387–1390.
150 C. Li, W. Wei, S. Fang, H. Wang, Y. Zhang, Y. Gui and R. Chen, *J. Power Sources*, 2010, **195**, 2939–2944.
151 C. Guan, X. Wang, Q. Zhang, Z. Fan, H. Zhang and H. J. Fan, *Nano Lett.*, 2014, **14**, 4852–4858.
152 J. Y. Huang, L. Zhong, C. M. Wang, J. P. Sullivan, W. Xu, L. Q. Zhang, S. X. Mao, N. S. Hudak, X. H. Liu,

Open Access Article. Published on 04 January 2021. Downloaded on 9/15/2024 1:15:01 AM.
This article is licensed under a Creative Commons Attribution 3.0 Unported Licence.

A. Subramanian, H. Fan, L. Qi, A. Kushima and J. Li, *Science*, 2010, **330**, 1515–1520.
153 R. Thomas and G. Mohan Rao, *J. Mater. Chem. A*, 2015, **3**, 274–280.
154 J. Liu, Y. Li, X. Huang, R. Ding, Y. Hu, J. Jiang and L. Liao, *J. Mater. Chem.*, 2009, **19**, 1859–1864.
155 X. W. Lou and H. C. Zeng, *Chem. Mater.*, 2002, **14**, 4781–4789.
156 J. S. Chen, Y. L. Cheah, S. Madhavi and X. W. Lou, *J. Phys. Chem. C*, 2010, **114**, 8675–8678.
157 X. Wang, W. Liu, H. Yang, X. Li, N. Li, R. Shi, H. Zhao and J. Yu, *Acta Mater.*, 2011, **59**, 1291–1299.
158 W. Zhang, L. L. Feng, H. Y. Chen and Y. Y. Zhang, *Nano*, 2019, **14**, 1950109.
159 F. Paraguay-Delgado, W. Antunez-Flores, M. Miki-Yoshida, A. Aguilar-Elguezaba, P. Santiago, R. Diaz and J. A. Ascencio, *Nanotechnology*, 2005, **16**, 688–694.
160 S. Ding, J. S. Chen and X. W. Lou, *Chem.–Asian J.*, 2011, **6**, 2278–2281.
161 N. Du, H. Zhang, B. Chen, X. Ma, X. Huang, J. Tu and D. Yang, *Mater. Res. Bull.*, 2009, **44**, 211–215.
162 X. Wang, J. Li, Z. Chen, L. Lei, X. Liao, X. Huang and B. Shi, *J. Mater. Chem. A*, 2016, **4**, 18783–18791.
163 B. Cheng, J. M. Russell, W. S. Shi, L. Zhang and E. T. Samulski, *J. Am. Chem. Soc.*, 2004, **126**, 5972–5973.
164 G. Xi and J. Ye, *Inorg. Chem.*, 2010, **49**, 2302–2309.
165 L. Tan, M. S. Wang, Y. J. Liu, X. C. Xiao, L. Z. Fan and Y. D. Wang, *Mater. Technol.*, 2013, **27**, 191–195.
166 Z.-S. Wu, W. Ren, L. Wen, L. Gao, J. Zhao, Z. Chen, G. Zhou, F. Li and H.-M. Cheng, *ACS Nano*, 2010, **4**, 3187–3194.
167 Q. Zhao, L. Ma, Q. Zhang, C. Wang and X. Xu, *J. Nanomater.*, 2015, **2015**, 850147.
168 J. Ye, H. Zhang, R. Yang, X. Li and L. Qi, *Small*, 2010, **6**, 296–306.
169 V. Kumar, J. H. Kim, C. Pendyala, B. Chernomordik and M. K. Sunkara, *J. Phys. Chem. C*, 2008, **112**, 17750–17754.
170 Y. Han, X. Wu, Y. Ma, L. Gong, F. Qu and H. Fan, *CrystEngComm*, 2011, **13**, 3506–3510.
171 S. Ding, D. Luan, F. Y. Boey, J. S. Chen and X. W. Lou, *Chem. Commun.*, 2011, **47**, 7155–7157.
172 D. Wang, X. Li, J. Wang, J. Yang, D. Geng, R. Li, M. Cai, T.-K. Sham and X. Sun, *J. Phys. Chem. C*, 2012, **116**, 22149–22156.
173 B. Zhao, S.-Y. Huang, T. Wang, K. Zhang, M. M. F. Yuen, J.-B. Xu, X.-Z. Fu, R. Sun and C.-P. Wong, *J. Power Sources*, 2015, **298**, 83–91.
174 L. Zhan, X. Zhou, J. Luo and X. Ning, *Ceram. Int.*, 2019, **45**, 6931–6936.
175 S. Hao, Y. Sun, Y. Liu, Y. Zhang and G. Hu, *J. Alloys Compd.*, 2016, **689**, 587–592.
176 S. Ramasamy, P. Nagamony and V. Chinnuswamy, *Mater. Lett.*, 2018, **218**, 295–298.
177 L.-L. Xing, Y.-Y. Zhao, J. Zhao, Y.-X. Nie, P. Deng, Q. Wang and X.-Y. Xue, *J. Alloys Compd.*, 2014, **586**, 28–33.
178 G. Z. Xing, Y. Wang, J. I. Wong, Y. M. Shi, Z. X. Huang, S. Li and H. Y. Yang, *Appl. Phys. Lett.*, 2014, **105**, 143905.
179 L. S. Fan, Z. K. Guo, Y. Zhang, X. Y. Zhang, M. X. Wang, Y. Y. Yin, N. Q. Zhang and K. N. Sun, *Mater. Today Energy*, 2019, **14**, 6.
180 D. Y. A. Esquivel, R. K. Brown, S. Knohl and U. Schroeder, *ChemElectroChem*, 2020, **7**, 1851–1859.
181 Y. Fu and A. Manthiram, *Nano Energy*, 2013, **2**, 1107–1112.
182 X. Meng, J. Zhang, Y. Wang and H. Liu, *Acta Chim. Sin.*, 2012, **70**, 812–816.
183 L. Jabbour, M. Destro, C. Gerbaldi, D. Chaussy, N. Penazzi and D. Beneventi, *J. Mater. Chem.*, 2012, **22**, 3227–3233.
184 L. Chang, Z. Yi, Z. Wang, L. Wang and Y. Cheng, *Appl. Surf. Sci.*, 2019, **484**, 646–654.
185 M.-S. Wang, Z.-Q. Wang, Z.-L. Yang, Y. Huang, J. Zheng and X. Li, *Electrochim. Acta*, 2017, **240**, 7–15.
186 R. Jia, J. Yue, Q. Xia, J. Xu, X. Zhu, S. Sun, T. Zhai and H. Xia, *Energy Storage Mater.*, 2018, **13**, 303–311.
187 L. Fan, Z. Guo, Y. Zhang, X. Zhang, M. Wang, Y. Yin, N. Zhang and K. Sun, *Mater. Today Energy*, 2019, **14**, E28–E62.
188 L. Vayssieres, *Adv. Mater.*, 2003, **15**, 464–466.
189 W.-w. Zhan, Q. Kuang, J.-z. Zhou, X.-j. Kong, Z.-x. Xie and L.-s. Zheng, *J. Am. Chem. Soc.*, 2013, **135**, 1926–1933.
190 J. Liu, S. Z. Qiao, S. B. Hartono and G. Q. Lu, *Angew. Chem., Int. Ed.*, 2010, **49**, 4981–4985.
191 J. Liu, T. Yang, D.-W. Wang, G. Q. Lu, D. Zhao and S. Z. Qiao, *Nat. Commun.*, 2013, **4**, 2798.
192 H. X. Yang, J. F. Qian, Z. X. Chen, X. P. Ai and Y. L. Cao, *J. Phys. Chem. C*, 2007, **111**, 14067–14071.
193 C.-Y. Chang-Chien, C.-H. Hsu, T.-Y. Lee, C.-W. Liu, S.-H. Wu, H.-P. Lin, C.-Y. Tang and C.-Y. Lin, *Eur. J. Inorg. Chem.*, 2007, **2007**, 3798–3804.
194 Y. Yin, S. Xin, L. Wan, C. Li and Y. Guo, *Sci. China: Chem.*, 2012, **55**, 1314–1318.
195 L. Zhang, H. B. Wu, B. Liu and X. W. Lou, *Energy Environ. Sci.*, 2014, **7**, 1013–1017.
196 Y. Liu, H. Dong and M. L. Liu, *Adv. Mater.*, 2004, **16**, 353–356.
197 T. Wang, H. Xu, Y. Wang, Y. Zeng and B. Liu, *Mater. Lett.*, 2020, **264**, 127320.
198 L. Zhou, J. Zhang, Y. Wu, W. Wang, H. Ming, Q. Sun, L. Wang, J. Ming and H. N. Alshareef, *Adv. Energy Mater.*, 2019, **9**, 1902194.
199 J. S. Chen, C. M. Li, W. W. Zhou, Q. Y. Yan, L. A. Archer and X. W. Lou, *Nanoscale*, 2009, **1**, 280–285.
200 S. Liu, M. Xie, Y. Li, X. Guo, W. Ji, W. Ding and C. Au, *Sens. Actuators, B*, 2010, **151**, 229–235.
201 Y.-Z. Wu, S. Brahma, S.-C. Weng, C.-C. Chang and J.-L. Huang, *J. Alloys Compd.*, 2020, **818**, 152889.
202 G. D. Park, J.-K. Lee and Y. C. Kang, *Adv. Funct. Mater.*, 2017, **27**, 1603399.
203 G. D. Park, J. H. Kim and Y. C. Kang, *Nanoscale*, 2018, **10**, 13531–13538.
204 J. S. Cho and Y. C. Kang, *Small*, 2015, **11**, 4673–4681.
205 L. Liu, F. Xie, J. Lyu, T. Zhao, T. Li and B. G. Choi, *J. Power Sources*, 2016, **321**, 11–35.

 © 2021 The Author(s). Published by the Royal Society of Chemistry

Open Access Article. Published on 04 January 2021. Downloaded on 9/15/2024 1:15:01 AM.
This article is licensed under a Creative Commons Attribution 3.0 Unported Licence.

206 H. Hu, L. Wu, P. Gebhardt, X. Zhang, A. Cherevan, B. Gerke, R. Pöttgen, A. Balducci, S. Passerini and D. Eder, *CrystEngComm*, 2017, **19**, 6454–6463.
207 W. Tian, C. Zhang, T. Zhai, S.-L. Li, X. Wang, M. Liao, K. Tsukagoshi, D. Golberg and Y. Bando, *Chem. Commun.*, 2013, **49**, 3739–3741.
208 Y. Kang, Z. Li, K. Xu, X. He, S. Wei and Y. Cao, *J. Alloys Compd.*, 2019, **779**, 728–734.
209 S. Ding, J. S. Chen, G. Qi, X. Duan, Z. Wang, E. P. Giannelis, L. A. Archer and X. W. Lou, *J. Am. Chem. Soc.*, 2011, **133**, 21–23.
210 J. Deng, Y. Chen, J. Ma, E. Zhang and T. Wang, *J. Nanosci. Nanotechnol.*, 2013, **13**, 4297–4301.
211 X. M. Yin, C. C. Li, M. Zhang, Q. Y. Hao, S. Liu, L. B. Chen and T. H. Wang, *J. Phys. Chem. C*, 2010, **114**, 8084–8088.
212 S. P. Kim, M. Y. Choi and H. C. Choi, *Appl. Surf. Sci.*, 2015, **357**, 302–308.
213 Z. Lu and H. Wang, *CrystEngComm*, 2014, **16**, 550–555.
214 H. Song, N. Li, H. Cui and C. Wang, *Electrochim. Acta*, 2014, **120**, 46–51.
215 J. Deng, Y. Dai, Z. Xiao, S. Song, H. Dai, L. Li and J. Li, *Nanomaterials*, 2020, **10**, 249.
216 Q. H. Tian, Y. B. Chen, W. Zhang, Z. Y. Sui and L. Yang, *J. Alloys Compd.*, 2020, **820**, 8.
217 X. Zhou, L. Yu and X. W. Lou, *Nanoscale*, 2016, **8**, 8384–8389.
218 A. Yang, X. Tao, R. Wang, S. Lee and C. Surya, *Appl. Phys. Lett.*, 2007, **91**, 133110.
219 X.-H. Li, H.-C. Huang, L. Ling, X.-Y. Wang, J.-R. Zhang and L. Gao, *Chin. J. Inorg. Chem.*, 2011, **27**, 781–784.
220 M. Xia, H.-Y. Guo and B. Yang, *Fullerenes, Nanotubes, Carbon Nanostruct.*, 2018, **26**, 76–79.
221 P. Wu, N. Du, H. Zhang, J. Yu, Y. Qi and D. Yang, *Nanoscale*, 2011, **3**, 746–750.
222 G. Du, C. Zhong, P. Zhang, Z. Guo, Z. Chen and H. Liu, *Electrochim. Acta*, 2010, **55**, 2582–2586.
223 K. Liu, S. Zhu, X. Dong, H. Huang and M. Qi, *Adv. Mater. Interfaces*, 2020, **7**, 1901916.
224 Y.-H. Jin, K.-M. Min, S.-D. Seo, H.-W. Shim and D.-W. Kim, *J. Phys. Chem. C*, 2011, **115**, 22062–22067.
225 G. Liang, X. Sun, J. Lai, C. Wei, Y. Huang and H. Hu, *J. Electroanal. Chem.*, 2019, **853**, 113401.
226 Q. Tian, Y. Tian, Z. Zhang, L. Yang and S.-i. Hirano, *J. Power Sources*, 2015, **291**, 173–180.
227 M. Liu, S. Zhang, H. C. Dong, X. Chen, S. Gao, Y. P. Sun, W. H. Li, J. Q. Xu, L. W. Chen, A. B. Yuan and W. Lu, *ACS Sustainable Chem. Eng.*, 2019, **7**, 4195–4203.
228 Q. Liu, Y. Dou, B. Ruan, Z. Sun, S. L. Chou and S. X. Dou, *Chemistry*, 2016, **22**, 5853–5857.
229 Y. Wan, Y. Sha, W. Deng, Q. Zhu, Z. Chen, X. Wang, W. Chen, G. Xue and D. Zhou, *Electrochim. Acta*, 2015, **167**, 69–74.
230 F. R. He, Q. Xu, B. P. Zheng, J. Zhang, Z. G. Wu, Y. J. Zhong, Y. X. Chen, W. Xiang, B. H. Zhong and X. D. Guo, *RSC Adv.*, 2020, **10**, 6035–6042.
231 L. Yuan, K. Konstantinov, G. X. Wang, H. K. Liu and S. X. Dou, *J. Power Sources*, 2005, **146**, 180–184.
232 H. Liu, D. Long, X. Liu, W. Qiao, L. Zhan and L. Ling, *Electrochim. Acta*, 2009, **54**, 5782–5788.
233 J. Shi, N. Lin, D. Liu, Y. Wang and H. Lin, *J. Electroanal. Chem.*, 2020, **857**, 113634.
234 X. Sun, J. Liu and Y. Li, *Chem. Mater.*, 2006, **18**, 3486–3494.
235 H. Qiao, Z. Zheng, L. Zhang and L. Xiao, *J. Mater. Sci.*, 2008, **43**, 2778–2784.
236 X. Tao, Q. Tian, L. Yang and Y. Xiang, *Mater. Lett.*, 2017, **202**, 107–110.
237 P. Wu, N. Du, H. Zhang, C. Zhai and D. Yang, *ACS Appl. Mater. Interfaces*, 2011, **3**, 1946–1952.
238 Y. Chen, Q. Z. Huang, J. Wang, Q. Wang and J. M. Xue, *J. Mater. Chem.*, 2011, **21**, 17448–17453.
239 M.-S. Wang, M. Lei, Z.-Q. Wang, X. Zhao, J. Xu, W. Yang, Y. Huang and X. Li, *J. Power Sources*, 2016, **309**, 238–244.
240 Z.-G. Wu, J.-T. Li, Y.-J. Zhong, J. Liu, X.-D. Guo, L. Huang, B.-H. Zhong and S.-G. Sun, *J. Alloys Compd.*, 2015, **620**, 407–412.
241 X. Wang, H. Fan, P. Ren and M. Li, *RSC Adv.*, 2014, **4**, 10284–10289.
242 X. Zhao, T. Wen, J. Zhang, J. Ye, Z. Ma, H. Yuan, X. Ye and Y. Wang, *RSC Adv.*, 2017, **7**, 21678–21685.
243 J. Yuan, C. Chen, Y. Hao, X. Zhang, B. Zou, R. Agrawal, C. Wang, H. Yu, X. Zhu, Y. Yu, Z. Xiong, Y. Luo, H. Li and Y. Xie, *J. Alloys Compd.*, 2017, **691**, 34–39.
244 C. Ma, W. Zhang, Y. S. He, Q. Gong, H. Che and Z. F. Ma, *Nanoscale*, 2016, **8**, 4121–4126.
245 S.-L. Yang, B.-H. Zhou, M. Lei, L.-P. Huang, J. Pan, W. Wu and H.-B. Zhang, *Chin. Chem. Lett.*, 2015, **26**, 1293–1297.
246 Yiliguma, Z. Wang, C. Yang, A. Guan, L. Shang, A. M. Al-Enizi, L. Zhang and G. Zheng, *J. Mater. Chem. A*, 2018, **6**, 20121–20127.
247 S. Nam, S. Kim, S. Wi, H. Choi, S. Byun, S.-M. Choi, S.-I. Yoo, K. T. Lee and B. Park, *J. Power Sources*, 2012, **211**, 154–160.
248 X. Ji, X. Huang, J. Liu, J. Jiang, X. Li, R. Ding, Y. Hu, F. Wu and Q. Li, *Nanoscale Res. Lett.*, 2010, **5**, 649–653.
249 L. Yu, D. Cai, H. Wang and M.-M. Titirici, *RSC Adv.*, 2013, **3**, 17281–17286.
250 X. W. Lou, J. S. Chen, P. Chen and L. A. Archer, *Chem. Mater.*, 2009, **21**, 2868–2874.
251 F. M. Courtel, E. A. Baranova, Y. Abu-Lebdeh and I. J. Davidson, *J. Power Sources*, 2010, **195**, 2355–2361.
252 G.-L. Xu, S.-R. Chen, J.-T. Li, F.-S. Ke, L. Huang and S.-G. Sun, *J. Electroanal. Chem.*, 2011, **656**, 185–191.
253 W. Zhang and H. Liu, *Neurocomputing*, 2017, **247**, 183–191.
254 C. Hernández-Rentero, V. Marangon, M. Olivares-Marín, V. Gómez-Serrano, Á. Caballero, J. Morales and J. Hassoun, *J. Colloid Interface Sci.*, 2020, **573**, 396–408.
255 Y. Dou, X. Liu, K. Yu, X. Wang, W. Liu, J. Liang and C. Liang, *Diamond Relat. Mater.*, 2019, **98**, 107514.
256 L.-L. Hu, L.-P. Yang, D. Zhang, X.-S. Tao, C. Zeng, A.-M. Cao and L.-J. Wan, *Chem. Commun.*, 2017, **53**, 11189–11192.
257 Q. Tian, F. Zhang, W. Zhang and L. Yang, *Electrochim. Acta*, 2019, **307**, 393–402.

Open Access Article. Published on 04 January 2021. Downloaded on 9/15/2024 1:15:01 AM.
This article is licensed under a Creative Commons Attribution 3.0 Unported Licence.

258 Z. Rujia, Z. Zhang, L. Jiang, K. Xu, Q. Tian, S. Xue, J. Hu, Y. Bando and D. Golberg, *J. Mater. Chem.*, 2012, **22**, 19196–19201.
259 W. Zhang, M. Li, X. Xiao, X. Huang, Y. Jiang, X. Fan and L. Chen, *J. Alloys Compd.*, 2017, **727**, 1–7.
260 Z. S. Wu, Y. Sun, Y. Z. Tan, S. Yang, X. Feng and K. Mullen, *J. Am. Chem. Soc.*, 2012, **134**, 19532–19535.
261 S. Stankovich, D. A. Dikin, R. D. Piner, K. A. Kohlhaas, A. Kleinhammes, Y. Jia, Y. Wu, S. T. Nguyen and R. S. Ruoff, *Carbon*, 2007, **45**, 1558–1565.
262 A. H. Castro Neto, F. Guinea, N. M. R. Peres, K. S. Novoselov and A. K. Geim, *Rev. Mod. Phys.*, 2009, **81**, 109–162.
263 A. K. Geim, *Science*, 2009, **324**, 1530–1534.
264 S.-y. Zuo, Z.-g. Wu, S.-k. Li, D. Yan, Y.-h. Liu, F.-y. Wang, R.-f. Zhuo, B.-s. Geng, J. Wang and P.-x. Yan, *RSC Adv.*, 2017, **7**, 18054–18059.
265 D. Zhou, X. Li, L.-Z. Fan and Y. Deng, *Electrochim. Acta*, 2017, **230**, 212–221.
266 M. Zhang, Z. Sun, T. Zhang, D. Sui, Y. Ma and Y. Chen, *Carbon*, 2016, **102**, 32–38.
267 Z. Li, G. Wu, S. Deng, S. Wang, Y. Wang, J. Zhou, S. Liu, W. Wu and M. Wu, *Chem. Eng. J.*, 2016, **283**, 1435–1442.
268 J. Han, D. Kong, W. Lv, D. M. Tang, D. Han, C. Zhang, D. Liu, Z. Xiao, X. Zhang, J. Xiao, X. He, F. C. Hsia, C. Zhang, Y. Tao, D. Golberg, F. Kang, L. Zhi and Q. H. Yang, *Nat. Commun.*, 2018, **9**, 402.
269 S. Shi, T. Deng, M. Zhang and G. Yang, *Electrochim. Acta*, 2017, **246**, 1104–1111.
270 Z.-S. Wu, W. Ren, L. Xu, F. Li and H.-M. Cheng, *ACS Nano*, 2011, **5**, 5463–5471.
271 D. D. Liu, Z. Y. Wei, B. Zhong, L. M. Liu, T. Zhang, X. M. Duan, M. Chen, H. T. Wang and X. X. Huang, *Appl. Surf. Sci.*, 2020, **519**, 5.
272 Y. Huang, R. Yu, G. Mao, W. Yu, Z. Ding, Y. Cao, J. Zheng, D. Chu and H. Tong, *J. Alloys Compd.*, 2020, **841**, 155670.
273 H. Zhang and S. Liu, *J. Alloys Compd.*, 2020, **842**, 155873.
274 K. Wang and Z. Li, *J. Nanosci. Nanotechnol.*, 2020, **20**, 7673–7679.
275 D. Liu, Z. Wei, B. Zhong, L. Liu, T. Zhang, X. Duan, M. Chen, H. Wang and X. Huang, *Appl. Surf. Sci.*, 2020, **519**, 146190.
276 X. Zuo, B. Li, K. Chang, H. Tang and Z. Chang, *RSC Adv.*, 2017, **7**, 53126–53134.
277 D. Usachov, O. Vilkov, A. Gruneis, D. Haberer, A. Fedorov, V. K. Adamchuk, A. B. Preobrajenski, P. Dudin, A. Barinov, M. Oehzelt, C. Laubschat and D. V. Vyalikh, *Nano Lett.*, 2011, **11**, 5401–5407.
278 H. Song, N. Li, H. Cui and C. Wang, *Nano Energy*, 2014, **4**, 81–87.
279 X. Zhou, L. J. Wan and Y. G. Guo, *Adv. Mater.*, 2013, **25**, 2152–2157.
280 N. Wu, W. Du, X. Gao, L. Zhao, G. Liu, X. Liu, H. Wu and Y. B. He, *Nanoscale*, 2018, **10**, 11460–11466.
281 J. P. Paraknowitsch and A. Thomas, *Energy Environ. Sci.*, 2013, **6**, 2839–2855.
282 K. Wu, B. Shi, L. Qi, Y. Mi, B. Zhao, C. Yang, Q. Wang, H. Tang, J. Lu, W. Liu and H. Zhou, *Electrochim. Acta*, 2018, **291**, 24–30.
283 U. N. Maiti, W. J. Lee, J. M. Lee, Y. Oh, J. Y. Kim, J. E. Kim, J. Shim, T. H. Han and S. O. Kim, *Adv. Mater.*, 2014, **26**, 40–67.
284 A. Verchere, S. Mishra, E. Jeanneau, H. Guillon, J.-M. Decams and S. Daniele, *Inorg. Chem.*, 2020, **59**, 7167–7180.
285 Y. Sun, S. Cheng, Z. Yu, L. Li, C. Li and J. Yang, *J. Alloys Compd.*, 2020, **834**, 155184.
286 M. Maleki, *Acta Phys. Pol., A*, 2020, **137**, 272–275.
287 W. Wang, Y. Liu and S. Liu, *Cryst. Growth Des.*, 2020, **20**, 2742–2752.
288 C. R. Ma, W. M. Zhang, Y. S. He, Q. Gong, H. Y. Che and Z. F. Ma, *Nanoscale*, 2016, **8**, 4121–4126.
289 L. Wen, F. Li and H.-M. Cheng, *Adv. Mater.*, 2016, **28**, 4306–4337.
290 B. A. Zhang, Q. B. Zheng, Z. D. Huang, S. W. Oh and J. K. Kim, *Carbon*, 2011, **49**, 4524–4534.
291 J. Wang, F. Fang, T. Yuan, J. Yang, L. Chen, C. Yao, S. Zheng and D. Sun, *ACS Appl. Mater. Interfaces*, 2017, **9**, 3544–3553.
292 S. K. Kulshreshtha, M. M. Gadgil and R. Sasikala, *Catal. Lett.*, 1996, **37**, 181–185.
293 A. Jayalakshmi, N. Venugopal, K. P. Raja and M. M. Rao, *J. Power Sources*, 2006, **158**, 1538–1543.
294 S.-H. Shin, J.-M. Song, S.-W. Kim, J.-K. Shin, S.-M. Lee, J.-C. Ro and S.-J. Suh, *Phys. Status Solidi A*, 2020, **217**, 1900996.
295 D. Shao, X. Zhang, Z. Wang, Y. Zhang, G. Tan and W. Yan, *Appl. Surf. Sci.*, 2020, **515**, 146003.
296 D. Shao, Y. Zhang, W. Lyu, X. Zhang, G. Tan, H. Xu and W. Yan, *J. Hazard. Mater.*, 2020, **390**, 122174.
297 M. Liu, H. Fan, O. Zhuo, J. Chen, Q. Wu, L. Yang, L. Peng, X. Wang, R. Che and Z. Hu, *Nano Energy*, 2020, **68**, 104368.
298 G. Luo, W. Liu, S. Zeng, C. Zhang, X. Yu, Y. Fang and L. Sun, *Electrochim. Acta*, 2015, **184**, 219–225.
299 Y. Liu, Y. Jiao, B. Yin, S. Zhang, F. Qu and X. Wu, *J. Mater. Chem. A*, 2015, **3**, 3676–3682.
300 Q. Tian, J. Yan, L. Yang and J. Chen, *Electrochim. Acta*, 2018, **282**, 38–47.
301 H. Xie, M. Chen and L. Wu, *Small*, 2017, **13**, 1604283.
302 H. Yang, T. Song, S. Lee, H. Han, F. Xia, A. Devadoss, W. Sigmund and U. Paik, *Electrochim. Acta*, 2013, **91**, 275–281.
303 J. S. Chen, C. M. Li, W. W. Zhou, Q. Y. Yan, L. A. Archer and X. W. Lou, *Nanoscale*, 2009, **1**, 280–285.
304 Y. Wang, J. Xu, H. Wu, M. Xu, Z. Peng and G. Zheng, *J. Mater. Chem.*, 2012, **22**, 21923–21927.
305 D.-F. Zhang, L.-D. Sun, C.-J. Jia, Z.-G. Yan, L.-P. You and C.-H. Yan, *J. Am. Chem. Soc.*, 2005, **127**, 13492–13493.
306 W.-W. Wang, *Mater. Res. Bull.*, 2008, **43**, 2055–2059.
307 W. Zhou, C. Cheng, J. Liu, Y. Y. Tay, J. Jiang, X. Jia, J. Zhang, H. Gong, H. H. Hng, T. Yu and H. J. Fan, *Adv. Funct. Mater.*, 2011, **21**, 2439–2445.
308 Z. X. Chen, M. Zhou, Y. L. Cao, X. P. Ai, H. X. Yang and J. Liu, *Adv. Energy Mater.*, 2012, **2**, 95–102.

 © 2021 The Author(s). Published by the Royal Society of Chemistry

Open Access Article. Published on 04 January 2021. Downloaded on 9/15/2024 1:15:01 AM.
This article is licensed under a Creative Commons Attribution 3.0 Unported Licence.

309 T. Yuan, Y. Jiang, Y. Li, D. Zhang and M. Yan, *Electrochim. Acta*, 2014, **136**, 27–32.
310 W. Wu, Y. Zhao, J. Li, C. Wu and L. Guan, *J. Energy Chem.*, 2014, **23**, 376–382.
311 J. Guo, H. Zhu, Y. Sun, L. Tang and X. Zhang, *J. Mater. Chem. A*, 2016, **4**, 16101–16107.
312 G. D. Park, J. K. Lee and Y. C. Kang, *J. Mater. Chem. A*, 2017, **5**, 25319–25327.
313 B.-R. Koo, D.-H. Lee, H.-J. Ahn and Y.-E. Sung, *J. Nanosci. Nanotechnol.*, 2016, **16**, 10558–10562.
314 J. Ma, J. Li, S. Yang, H. Lu, L. Liu and R. Wang, *J. Power Sources*, 2020, **453**, 227866.
315 Y. Qi, H. Zhang, N. Du, C. Zhai and D. Yang, *RSC Adv.*, 2012, **2**, 9511–9516.
316 J. Hou, C. Cao, F. Idrees and X. Ma, *ACS Nano*, 2015, **9**, 2556–2564.
317 Y. N. Sun, M. Goktas, L. Zhao, P. Adelhelm and B. H. Han, *J. Colloid Interface Sci.*, 2020, **572**, 122–132.
318 X. Li, Y. Zhang, T. Li, Q. Zhong, H. Li and J. Huang, *Electrochim. Acta*, 2014, **147**, 40–46.
319 W. Tao, M. Wang, B. Zhu, W. Huo, R. Yang, H. Xiong, H. Tang, Z. Wei and Y. Wang, *Electrochim. Acta*, 2020, **334**, 135569.
320 B. Huang, Z. Pan, X. Su and L. An, *J. Power Sources*, 2018, **395**, 41–59.
321 H. Zhou, Y. Zhong, Z. He, L. zhang, J. Wang, J. Zhang and C.-n. Cao, *Appl. Surf. Sci.*, 2014, **314**, 1–6.
322 J. Ding, X. Gao, L. Cha, M.-Q. Cai and J. Ma, *RSC Adv.*, 2016, **6**, 108310–108314.
323 Q. Tian, Z. Zhang, L. Yang and S.-i. Hirano, *RSC Adv.*, 2015, **5**, 40303–40309.
324 F. Yang, Y. Zhu, X. Li, C. Lai, W. Guo and J. Ma, *RSC Adv.*, 2015, **5**, 98717–98720.
325 Y. Xing, S. Wang, B. Fang, G. Song, D. P. Wilkinson and S. Zhang, *J. Power Sources*, 2018, **385**, 10–17.
326 R. D. Shannon, *Acta Crystallogr., Sect. A: Cryst. Phys., Diffr., Theor. Gen. Crystallogr.*, 1976, **32**, 751–767.
327 L. Zhou, H. Guo, T. Li, W. Chen, L. Liu, J. Qiao and J. Zhang, *Sci. Rep.*, 2015, **5**, 15252.
328 Z. Yang, G. Du, Z. Guo, X. Yu, Z. Chen, T. Guo and R. Zeng, *Nanoscale*, 2011, **3**, 4440–4447.
329 Z. Yi, Q. Han, P. Zan, Y. Cheng, Y. Wu and L. Wang, *J. Mater. Chem. A*, 2016, **4**, 12850–12857.
330 J. Y. Cheong, C. Kim, J. S. Jang and I.-D. Kim, *RSC Adv.*, 2016, **6**, 2920–2925.
331 A. Xu, X. Dai, K. Wei, W. Han, J. Li, X. Sun, J. Shen and L. Wang, *RSC Adv.*, 2017, **7**, 37806–37814.
332 L. Xu, Y. Wang and W. Zhang, *RSC Adv.*, 2019, **9**, 39242–39251.
333 Z. Yang, G. Du, Q. Meng, Z. Guo, X. Yu, Z. Chen, T. Guo and R. Zeng, *RSC Adv.*, 2011, **1**, 1834–1840.
334 H. Yoo, G. Lee and J. Choi, *RSC Adv.*, 2019, **9**, 6589–6595.
335 Z. Yang, Q. Meng, Z. Guo, X. Yu, T. Guo and R. Zeng, *J. Mater. Chem. A*, 2013, **1**, 10395–10402.
336 L. He, C. Wang, X. Yao, R. Ma, H. Wang, P. Chen and K. Zhang, *Carbon*, 2014, **75**, 345–352.
337 Z. Lu and H. Wang, *CrystEngComm*, 2014, **16**, 550–555.
338 Y. Tang, D. Wu, S. Chen, F. Zhang, J. Jia and X. Feng, *Energy Environ. Sci.*, 2013, **6**, 2447–2451.
339 S. Bai and X. Shen, *RSC Adv.*, 2012, **2**, 64–98.
340 R. K. Singh, R. Kumar and D. P. Singh, *RSC Adv.*, 2016, **6**, 64993–65011.
341 H. F. Xiang, Z. D. Li, K. Xie, J. Z. Jiang, J. J. Chen, P. C. Lian, J. S. Wu, Y. Yu and H. H. Wang, *RSC Adv.*, 2012, **2**, 6792–6799.
342 G. Zhao, T. Wen, C. Chen and X. Wang, *RSC Adv.*, 2012, **2**, 9286–9303.
343 A. Abbasnezhad, H. Asgharzadeh, A. Ansari Hamedani and S. Hayat Soytas, *Dalton Trans.*, 2020, **49**, 5890–5897.
344 S. Bai, S. Chen, X. Shen, G. Zhu and G. Wang, *RSC Adv.*, 2012, **2**, 10977–10984.
345 L. Tao, J. Zai, K. Wang, Y. Wan, H. Zhang, C. Yu, Y. Xiao and X. Qian, *RSC Adv.*, 2012, **2**, 3410–3415.
346 C. Y. Du, M. Chen, X. Y. Cao, G. P. Yin and P. F. Shi, *Electrochem. Commun.*, 2009, **11**, 496–498.
347 J. Zhao, W. Shan, X. Xia, Q. Wang and L. Xing, *Sci. China: Technol. Sci.*, 2014, **57**, 1081–1084.
348 J. Sun, Q. Wang, Q. Wang, D. A. Zhang, L. L. Xing and X. Y. Xue, *Sci. Adv. Mater.*, 2016, **8**, 1280–1285.
349 R. Cai, X. Yu, X. Liu and Z. Shao, *J. Power Sources*, 2010, **195**, 8244–8250.
350 Y. Hui, L. Cao, Z. Xu, J. Huang, H. Ouyang and J. Li, *J. Electroanal. Chem.*, 2016, **763**, 45–50.
351 J. Gao, C. Jiang, J. Ying and C. Wan, *J. Power Sources*, 2006, **155**, 364–367.
352 K. Song, D.-H. Seo, M. R. Jo, Y.-I. Kim, K. Kang and Y.-M. Kang, *J. Phys. Chem. Lett.*, 2014, **5**, 1368–1373.
353 F. Mueller, D. Bresser, V. S. K. Chakravadhanula and S. Passerini, *J. Power Sources*, 2015, **299**, 398–402.
354 A. Chen, S. J. Xia, H. Y. Pan, J. H. Xi, H. Y. Qin, H. W. Lu and Z. G. Ji, *J. Electroanal. Chem.*, 2018, **824**, 169–174.
355 Y. H. Cui and Y. J. Feng, *J. Mater. Sci.*, 2005, **40**, 4695–4697.
356 V. Subramanian, K. I. Gnanasekar and B. Rambabu, *Solid State Ionics*, 2004, **175**, 181–184.
357 T. Jia, J. Chen, Z. Deng, F. Fu, J. Zhao, X. Wang and F. Long, *Mater. Sci. Eng., B*, 2014, **189**, 32–37.